Progress in Additive Manufacturing (2026) 11:6491–6517
https://doi.org/10.1007/s40964-026-01728-2

REVIEW

Additive manufacturing of refractory niobium alloys: a review of processing, properties, modeling, and applications

Thomas Keller[1] · Cheng Zeng[1] · Nathan Post[1] · Jack Lesko[1] · Andrew Neils[1]

Received: 10 April 2025 / Accepted: 22 April 2026 / Published online: 7 May 2026

Abstract
Alloys and intermetallics based on the refractory element niobium (Nb) have proven useful in many high-temperature applications requiring high strength, ductility, and corrosion resistance. However, its high raw material cost, a high affinity for oxygen embrittlement, and exceptional thermal properties and strength in harsh environments makes the processing of Nb alloys through conventional techniques difficult. Recent advances in additive manufacturing (AM) of these materials have demonstrated mechanical properties comparable to those produced by conventional casting. Furthermore, high-throughput computing, machine learning, and automation have opened up unprecedented opportunities to overcome AM processing challenges like process window selection, oxidation mitigation, and porosity defects. Thus, this review describes the AM processes that have been applied to Nb alloys, assesses their microstructures, and explains their effects on the mechanical and physical properties. It also highlights how computation can aid in the design and processing of Nb alloys for AM. Ultimately, it provides a roadmap for processing Nb alloys via AM, highlighting their most promising applications as well as where further research is needed.

Keywords Additive manufacturing · Niobium · Refractory alloy · Materials design · Data analytics · Oxidation

1 Introduction

There is a rising demand for materials that exhibit improved strength and stability in extreme applications including ultra-high-temperature environments. Refractory alloys, including niobium (Nb) based alloys, are recognized as one of the few metallic solutions for these demanding applications. While metal additive manufacturing (AM) processes have advanced significantly over the past few decades, the literature remains sparse regarding Nb alloy AM production. This review surveys the AM processes that have been used to fabricate Nb-based alloys, evaluates their effectiveness, and identifies unresolved manufacturing challenges that must still be addressed.

1.1 Niobium material properties

Refractory alloys are a class of materials known for their excellent high-temperature properties, making them well-suited for a range of applications in harsh environments such as nuclear reactors and aircraft engines. Refractory alloys are commonly defined as alloys composed of refractory elements that share the common properties of melting points above 2000 °C and high hardness at room temperature. This narrow definition includes the elements molybdenum (Mo), niobium (Nb), rhenium (Re), tantalum (Ta), and tungsten (W), and a broader definition can sometimes include elements with melting points above 1850 °C, such as chromium (Cr), hafnium (Hf), iridium (Ir), osmium (Os), rhodium (Rh), ruthenium (Ru), titanium (Ti), vanadium (V), and zirconium (Zr) [1]. In the aerospace sector, refractory alloys are known for their exceptional corrosion resistance, wear resistance, and strength at elevated temperatures up to

✉ Thomas Keller
t.keller@northeastern.edu

Cheng Zeng
cheng_zeng1@alumni.brown.edu

Nathan Post
n.post@northeastern.edu

Jack Lesko
j.lesko@northeastern.edu

Andrew Neils
a.neils@northeastern.edu

1 Northeastern University, Boston, USA

1400 –1800 °C [2–6]. However, applications of refractory alloys are impeded by their poor low-temperature ductility and, consequently, manufacturability. The inferior ductility can be attributed to partially filled d-orbitals in refractory elements, which result in the formation of covalent-like bonds and the formation of body-centered cubic (BCC) crystal structures [7]. Single-phase BCC refractory alloys are generally more susceptible to crack initiation during AM due to their less efficient slip systems and reduced ability to accommodate thermal stresses during cooling from their high melting point [8, 9]. The manufacturing difficulty can also be compounded by the presence of interstitial defects in the BCC lattice, like oxygen (O), that cause embrittlement and further diminish ductility [10, 11].

Among all refractory elements, pure Nb exhibits the highest ductility at room temperature with an elongation at break as high as 50%, forming a BCC crystal structure (*Im*(−3)*m* space group, $a = 0.33$ nm) with a bulk density of 8.6 g/cm^3 [12]. This ductility, despite being a BCC metal, is due largely to its low ductile to brittle transition temperature, below − 121 °C and increasing with loss of purity, which means that pure Nb remains in its ductile state in all but the most extreme low-temperature environments. However, this ductility drops to nearly zero when Nb contains as little as 1 at% O [13]. O sits interstitially in the BCC Nb unit cell, occupying octahedral sites as shown in Fig. 1 [14]. Pure Nb has a melting point of 2477 °C, a boiling point of 4744 °C, and a room temperature thermal conductivity of ~ 54 W/m·K [12]. It becomes superconductive below the critical temperature of − 263.9 °C, and is useful as a superconductor when alloyed with Al, Ga, GeAl, Sn, or Ti to improve performance [14, 15].

As it does not occur naturally in its pure elemental form, Nb is chemically extracted from iron-based (Fe) minerals and, consequently, has a relatively high raw material cost [17]. Brazil is the largest producer of Nb, supplying 90% of global production and holding 90% of the global reserves [18]. Canada is the second largest producer, with other smaller-scale producers in Australia, Russia, and Nigeria.

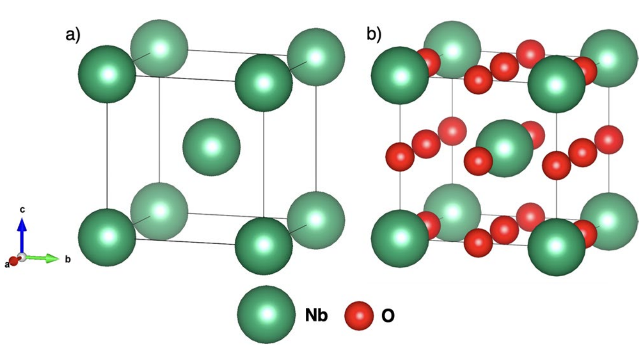

Fig. 1 The crystal structure of **a** BCC Nb and **b** BCC Nb with octahedral sites for interstitial O. Data from [14] and drawn with [16]

With supply concentrated in Brazil, future geopolitical or environmental risks could impact the supply chain. Hence, alternative sources and recycling efforts are likely to gain further attention [19]. Likewise, countries concerned about Nb supply security, like the U.S. and China, have considered or implemented strategic stockpiling to mitigate potential supply disruptions [20].

1.2 Applications of niobium alloys

Nb-C103 alloy, with a composition of Nb-10Hf-1Ti wt%, is the most widely used Nb alloy in conventional manufacturing and is used in rocket nozzles and jet engines [10, 21–23]. Another type of Nb alloy, Nb-521 (Nb-5 W-2Mo-1Zr wt%), is also used in propulsion systems [24]. Other commercial aerospace alloys include C3009 (Nb-30Hf-10 W wt%), C129Y (Nb-10Hf-10 W-0.1Y wt%), Cb752 (Nb-10 W-2.5Zr wt%), and FS85 (Nb-28Ta-10 W-1Zr wt%). These alloys demonstrate a favorable combination of low creep rates and high corrosion resistance at elevated temperatures. Common alloying elements of similar electronic structure to Nb, such as Hf, Mo, Ta, Ti, W, Zr, and Y have very high solid solubility in Nb; they substitutionally occupy the Nb sites while retaining the BCC structure [25]. Other useful Nb-based materials are intermetallic niobium silicide (Nb-Si) composites, which combine the ductility of the BCC Nb_{ss} (solid solution) with the strength, creep resistance, and oxidation resistance of silicide phases such as Nb_3Si and Nb_5Si_3 [26–28].

High-strength low-alloy steel is the most common use case of Nb in automotive, construction, and other infrastructure applications [29]. Nb is also used in nuclear applications in the form of niobium-zirconium (Nb-Zr), which has good resistance to neutron absorption and corrosion [30]. Similar to aerospace, Nb alloys can be found in the energy sector to enhance reliability and performance in high-temperature gas turbine components [31]. Lastly, Nb alloys are used in medical devices and implants, given their biocompatibility, corrosion resistance, and mechanical strength [32, 33]. Therefore, Nb alloys improve upon the mechanical properties of pure Nb while retaining high-temperature performance. Nevertheless, Nb can be easily oxidized, necessitating a protective coating for many applications to prevent catastrophic O embrittlement [10, 21]. Embrittlement from interstitial carbon, hydrogen, and nitrogen must also be mitigated in certain situations [13, 34]. Due to their unique low-temperature ductility, Nb alloys are more amenable to machining compared to other refractory alloys. Despite this, it is challenging to fabricate complex geometry Nb alloy parts at affordable costs using subtractive machining due to the large amount of expensive scrap material lost. This economic incentive therefore makes Nb alloys particularly suitable for AM and has motivated recent research into AM Nb parts with complex geometries such as rocket thrusters (Fig. 2) [35].

1.3 Additive manufacturing of niobium alloys

Compared to traditional casting and forging techniques, AM offers many advantages including greater design flexibility, less material waste, and faster prototyping. This is especially pertinent to actively cooled parts, such as rocket nozzles, that require internal coolant channels not possible with traditional manufacturing [36, 37]. Therefore, as an integrated part of Industry 4.0, AM opens up new opportunities in manufacturing Nb alloy parts for aerospace applications in an efficient and precise manner [38, 39]. For instance, powder bed fusion (PBF) and direct energy deposition (DED) have been extensively investigated to produce Nb alloys, including pure Nb, Nb-C103, Nb-521, Nb-Si, and Nb-1Zr [40–48].

As mentioned previously, Nb alloys have specific properties that make them challenging to process with AM. First, are their high raw material costs, necessitating an efficient use of AM feedstock in the design of each AM process to minimize waste. Second, are their exceptionally high melting points, requiring sufficiently high energy input to achieve a molten state in fusion-based AM processes. This can also lead to severe thermal gradients during AM, thus defects like lack of fusion and cracking must also be mitigated. Third, are their susceptibilities to oxidation embrittlement, which require careful control of the ambient atmosphere during AM and heat treatments. This is exceptionally important for powder-based AM techniques, due to the high surface area to volume ratio exhibited by powders that can lead to rapid oxidation. If these considerations are not made when designing an AM process for Nb alloys, then there will be an inevitable loss of their exceptional strength and ductility.

The inherent costs and material challenges of designing AM processes for Nb alloys make traditional trial-and-error approaches less feasible. However, thanks to advances in high-throughput computing and artificial intelligence (AI), materials design and process optimization for AM have reached an unprecedented level of utility [51–53]. Multi-scale simulations provide insights into the physical fundamentals of AM ranging from nano-scales to micro-scales and up to device scales [54, 55]. A variety of machine learning (ML) methods have been adopted to speed up materials simulations across this size spectrum [27, 56], optimize process parameters [57, 58] and create virtual entities like digital twins for faster materials qualification [54, 59]. However, this review finds that computational modeling techniques are notably understudied for AM of Nb alloys. Thus, there is a considerable opportunity to translate the success of computational modeling and ML from similar material systems into the AM design of Nb-based materials to rapidly optimize the quality and performance.

Although there are a number of reviews on AM refractory alloys in general [11, 38, 39], more specific AM techniques [23, 60] and specific alloys [61, 62], as well as computational modeling for AM [56–58, 63], there is no such a review that specially focuses on Nb alloys, and how simulation and ML techniques can be integrated into the design of such materials made by AM.

This review begins with a survey of the state-of-the-art in AM for Nb alloys, limiting the scope to alloys of > 50 at% Nb. This includes the processing of Nb alloys with different AM methods (Sect. 2) as well as their resulting material properties and microstructures (Sect. 3). These are followed by an examination of how modeling and ML can improve AM of Nb alloys (Sect. 4).

2 Additive manufacturing

2.1 Powder bed fusion

Powder bed fusion (PBF) methods for AM of Nb alloys use a focused energy source to convert a powder feedstock into a bulk material through selective melting. They can be

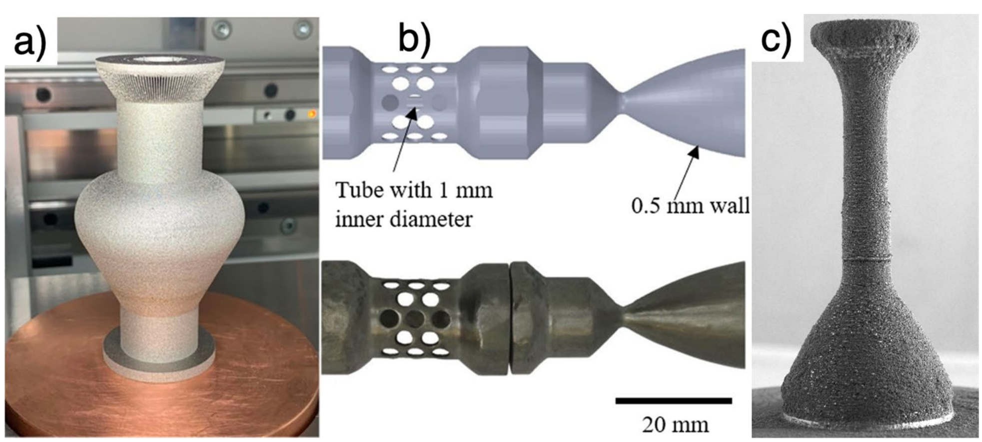

Fig. 2 Examples of Nb components manufactured with PBF AM: **a** a pure Nb superconducting radio frequency cavity, **b** a pure Nb rocket thruster alongside its computer-aided design (CAD) model above [49], **c** a Nb-C103 rocket thruster [10]. Images (**a**) and (**b**) reprinted under CC BY 4.0 license from Springer [50], (**c**) reprinted with permission from Springer

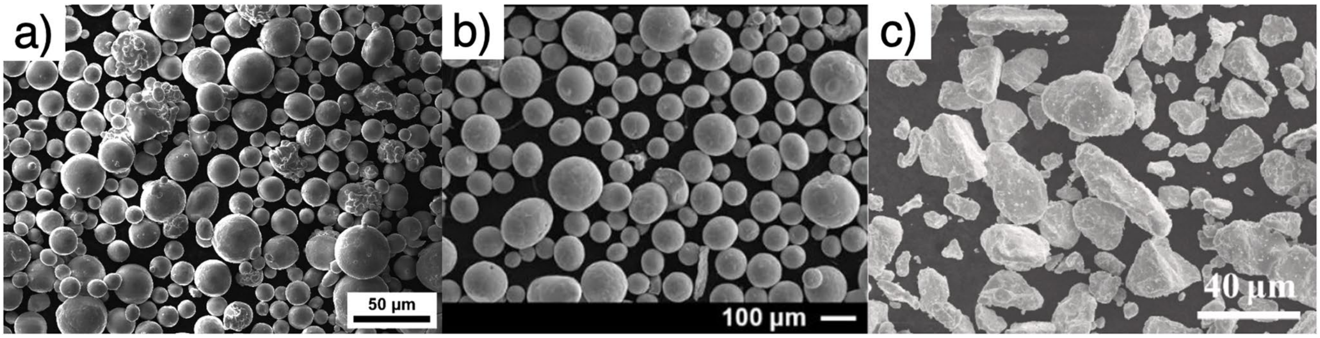

Fig. 3 Feedstock powder used in the production of Nb alloys in AM **a** gas-atomized Nb-C103 [66], **b** plasma spheroidized Nb-1Zr [65], **c** jet milled Nb-521 [24]. Reprinted with permission from (**a**) Springer, (**b**) reprinted under CC BY 4.0 license from MDPI [50] (**c**) reprinted with permission from Elsevier

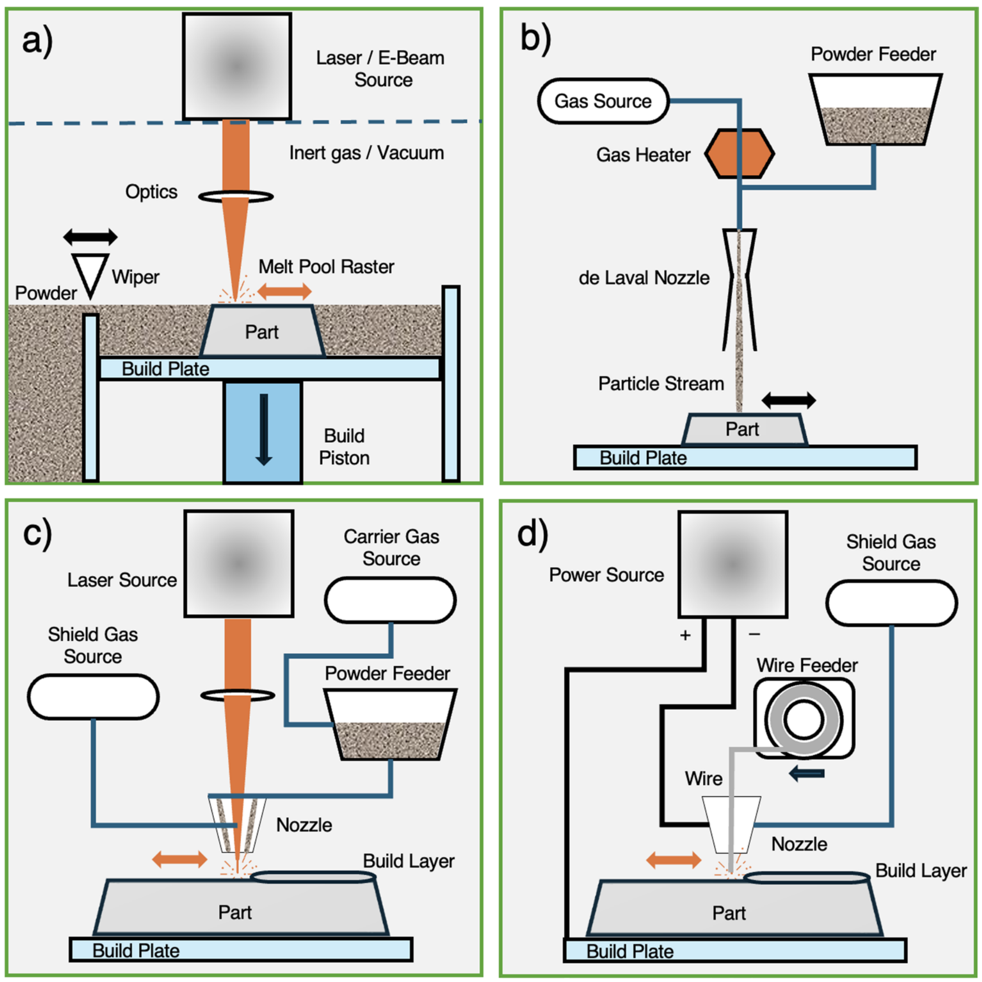

Fig. 4 Schematics of Nb alloy AM techniques: **a** laser powder bed fusion and electron beam powder bed fusion, **b** cold spray **c** laser powder direct energy deposition, **d** wire-arc direct energy deposition

broadly broken down into two main areas depending on the energy source: laser PBF (LPBF) and electron beam PBF (EPBF). In both techniques, the focused energy source is rastered across a powder bed (Fig. 3) spread flat atop a starting build plate (Fig. 4a). At each raster point, the powder bed experiences rapid melting followed by rapid cooling as the energy source moves on to the next raster location. After one entire raster pattern across the surface is complete, the build plate is lowered and another layer of powder is wiped across the surface so that a new layer can be selectively melted, building up the volume of solid material in three dimensions.

LPBF and EPBF primarily differ in the power of the directed energy beam, the speed of the raster, and the ambient conditions at which the melt fusion occurs [64]. For example, EPBF has the advantages of higher power output and raster speed compared to LPBF. However, EPBF requires a vacuum atmosphere partially backfilled with helium whereas LPBF can be performed at atmospheric pressure in an inert gas, typically argon or nitrogen. This makes LPBF systems simpler to operate, but EPBF systems can better prevent contamination in materials prone to oxidation embrittlement like Nb. In addition, the general particle size range of LPBF (15–65 µm) is smaller than that of EPBF (45–150 µm), giving it a higher surface area to volume ratio and making the EPBF feedstock powder relatively less prone to oxidation [46]. By performing de-focused raster passes of the electron beam over the surface prior to the first layer and in between layers, EPBF can be performed on a build plate and powder bed surface maintained at relatively high temperature under vacuum (≥ 1000 °C for refractory alloys [35]) whereas the build surface in LPBF cannot achieve such high temperatures due to heat loss to the ambient atmosphere. Therefore, the thermal gradient in LPBF is generally higher and the cooling rate is generally faster compared to EPBF. Broadly speaking, this means that EPBF better handles two of the inherent challenges of AM of Nb alloys: it has lower thermal gradients and is less prone to oxidation, meaning that the resulting parts may generally have fewer defects.

Because the powder bed must be wiped smooth into a flat layer with each increment in build height, both PBF methods require highly spherical and flowable feedstock powders of a controlled particle size distribution. Gas-atomization (GA) and plasma spheroidization (PS) have been shown to be viable methods to prepare powder feedstock for PBF of Nb alloys, although jet-milling may also be suitable in some cases if a high particle sphericity and flowability can be achieved (Fig. 3) [10, 24, 65].

A useful metric for comparing LPBF processing conditions is to take the product of the variables of scan speed, hatch spacing, and layer thickness to calculate the volumetric build rate (VBR) in mm^3/s [49]. Dividing the laser power by the build rate gives the volumetric energy density (VED) in J/mm^3 [67]. These metrics do not precisely track the heat flow dynamics of the melt pool, nor include the actual laser beam spot size, but they provide an approximation of the heating and cooling behavior. However unlike for LPBF, process parameters for EPBF are less consistently reported, making it difficult to compare across different experiments and calculate VBR or VED. For example, rather than having a distinct laser power, the energy input for EPBF is an electron beam with a beam voltage (kV) and beam current (mA), where the product of the two equals the power (W) of the electron beam. Additionally, the electromagnetic optics have a focus or offset current that influences the beam spot size. Fortunately, the majority of the EPBF market is dominated by only a few companies, namely GE Additive (formerly Arcam), JEOL, and Freemelt AB, all of which are generally run at a recommended 60 kV beam voltage and a focus offset of 30–50 mA [44, 46, 68].

Post-processing techniques can be used to further modify the material properties and microstructure after fusion. These techniques include compaction, to improve bulk density and minimize porosity, and annealing, to relieve retained thermal stress, remove defects, and increase grain size [69]. Given the high-temperature and high stress requirements of Nb alloys in aerospace applications, post-processing is a means to improve ductility and thermal conductivity and therefore reduce the likelihood of brittle failure [70].

2.1.1 Laser powder bed fusion

Several studies have used LPBF on Nb alloys, including pure Nb [2, 42, 49, 71, 72], Nb-521 [24, 40, 73], and Nb-C103 [22, 66, 74]. Comparing their processing parameters, different laser powers (110–350 W), layer thicknesses (0.02 –0.05 mm), scan speeds (250 mm/s–1000 mm/s) and hatch spacings (0.05–0.12 mm) resulted in a broad range of VBRs (0.4–2.4 mm^3/s) and VEDs (87.5–389 J/mm^3).

LPBF on pure Nb generally achieved a relative density of ≥ 98% [42], and as high as 99.9% when VED was ≥ 100 J/mm^3 [49, 72]. Nb-521 generally had a slightly lower density of 98.8–99.2% [24, 73] under similar VED values of ≥ 90 J/mm^3, due to an observed increase in porosity and the formation of low-density ZrO_2 precipitates. LPBF Nb-C103 reached a density of 99.1% at 121 J/mm^3 [22] and 99.9% at 169 J/mm^3 [66]. In Nb-521 and Nb-C103, lack of fusion defects, where heating is insufficient to fully close the voids between particles, were noted as the primary cause of low density. Therefore, a VED of > 150 J/mm^3 is needed to reach a sufficient relative density in most Nb alloys and a VED as high as 390 J/mm^3 does not appear to have a detrimental effect beyond slowing the VBR.

A limited number of studies have produced Nb-Si intermetallics via LPBF, particularly using $Nb_{52}Si_{18}Ti_{24}Cr_2Al_2Hf_2$ (98.3% relative density) [75] and $Nb_{76}Si_{18}Hf_5C_1$ (density not reported) [43]. In both cases, a multi-phase microstructure was obtained, containing a mixture of Nb_{ss}, Nb_5Si_3, and Nb_3Si phases, utilizing a VED of 63 J/mm^3 – 75 J/mm^3.

2.1.2 Electron beam powder bed fusion

As mentioned previously, VBR and VED are not well reported for EPBF of Nb. Despite this, useful insights can still be gained by comparing the processing conditions used to consolidate Nb-based feedstocks via EPBF [44–46, 65, 76–78]. In all studies where process conditions were reported, layer thicknesses were ~70 µm, with hatch spacing ranging from 100 to 200 µm.

The process variables that varied most between studies were beam power (600–1110 W), scanning speed (172–700 mm/s), and preheat temperature (610–1150 °C), which all influence the heat flow in and out of the part during AM. In the case of pure Nb, a 99.7% relative density was reported [44], whereas values of 99.2% and 99.8% relative density were reported for Nb-521 [45] and Nb-C103 [46], respectively. Similar to observations in LPBF of Nb-C103, EPBF builds using a beam current below 15 mA resulted in unmelted particles and lack of fusion defects, contributing to the lower relative density. When comparing EPBF processing of pure Nb and Nb-C103 at the same scanning speed of 300 mm/s, the energy input had to be greatly increased from the pure Nb (720 W and 610 °C powder bed preheat) [76] to Nb-C103 (1080 W and 1100 °C powder bed preheat) [46]to achieve similar build quality on the same type of Arcam EPBF instrument. Despite pure Nb having a slightly higher melting point and heat capacity than Nb-C103, the need for added energy input may be due to Nb-C103 having a lower thermal conductivity [79, 80]. Generally, a faster scanning speed, which increases the build speed as well as the cooling rate from melt, can be reasonably offset by a higher beam current and substrate preheat temperature to maintain build quality.

Gao et al. have reported the first use of EPBF to manufacture an Nb-Si intermetallic [77]. With a composition of Nb-26Ti-16Si-2.2Al–2Cr wt%, they produced a composite with roughly 33 vol% Nb-Ti solid solution and 67 vol% Nb_3Si phase.

2.2 Direct energy deposition

A third powder-based fusion method distinct from LPBF and EPBF is laser powder direct energy deposition (LPDED) (Fig. 4c). LPDED differs from LPBF in that the powder is deposited directly from a nozzle at the laser location rather than being wiped flat across a whole surface, eliminating the constraint of the build plate size [81]. This makes it possible to make large-format parts and repair existing parts by directly manufacturing onto non-flat surfaces. However, because the laser spot size is significantly larger than in LPBF, the microstructure and surface topology cannot be as finely controlled.

Direct energy deposition (DED) is possible through the powder feedstock method, LPDED, as well as with a wire feedstock and either a laser, plasma arc, or electron beam energy source. The simplest and most common arrangement is wire-arc DED (WADED), wherein a wire feedstock is deposited via a plasma arc, similar to conventional welding (Fig. 4d) [82]. The primary difference from welding is that the plasma source, wire feed rate, and deposition pattern are all automated, and a robotic arm is used to raster the arc and molten tip of the wire. WADED can be used on alloys that suffer from poor laser absorption due to reflectivity, such as Al and Cu, and the wire feedstock has the benefits of low material cost and high deposition efficiency compared to powder [83]. Like LPDED, it can produce large format parts and repair existing parts, with the highest build rate of the AM techniques in this review. However, because of the large wire feedstock and arc melt pool, the microstructure and surface topology in WADED are the least well controlled and post-process machining is almost always required to achieve net-shape [84].

Because of the large melt pool in DED, it generally has a slower cooling rate than PBF and thus solves one of the inherent challenges of AM of Nb alloys by lowering the thermal gradients and minimizing cracking [41, 85]. Additionally, the wire feedstock in WADED has a lower surface area to volume ratio than powder, minimizing the surface oxygen uptake in feedstock manufacturing [86]. However, DED is generally performed under a shielding gas rather than in a sealed inert gas or vacuum atmosphere and thus LPDED may introduce more oxygen contamination than PBF methods [70]. Thus, more research directly comparing the oxygen uptake using identical alloys and shielding gas are needed to fully understand this behavior.

2.2.1 Laser powder direct energy deposition

A handful of studies have explored LPDED AM of Nb alloys, including pure Nb [70], Nb-TiC [70], Nb-C103 [47, 87], and intermetallic Nb-Si [27, 48]. As mentioned previously, the laser spot size is much larger for LPDED compared to LPBF, which increases the size of the melt pool during scanning and lowers the special resolution. A larger melt pool generally slows down the cooling rate from melt and increases the grain size in the as-built material. This requires not only very high laser power, (800–1420 W) but also a relatively low scanning speed (13–14 mm/s) to fuse pure Nb, Nb-TiC, and Nb-C103. $Nb_{84}Si_{16}$ powder, on the other hand, has a melting point of 2080 °C, lower than pure Nb powder at 2470 °C, allowing for much higher reported scan speeds of 600 mm/s with a 900 W laser [26]. Relative densities of 99.9% and 98.9% were reported for LPDED Nb-C103 [47] and $Nb_{84}Si_{16}$ [48], respectively. Combining this with the aforementioned results from LPBF indicates that the multi-phase Nb-Si intermetallic composite struggles to match the density of Nb alloys by LPBF or LPDED, although the relative densities are similar to the more common technique of spark plasma sintering (99.2–99.6%) [26, 88]. Note that these general estimations are required because VED could not generally be calculated for LPDED, as the powder feed rate was reported instead of the layer thickness.

2.2.2 Wire arc direct energy deposition

Compared to LPDED, few peer-reviewed studies have explored WADED of Nb alloys. Islam et al. produced two studies on WADED of Nb-1Zr wt% under mixed 70% Ar and 30% He shielding gas [41, 85]. A W electrode with 180–220 A applied current was held 5 mm from the substrate and moved at 200 mm/min along with a 0.95 mm feedstock wire, resulting in a VED range of 138–168 J/mm^3, similar to LPBF of Nb. Unlike LPBF, they reported a microstructure free of cracks and porosity due to the larger melt pool and slower cooling rate from melt in WADED. However, they observed that increasing the VED led to a loss of spatial resolution, as the melt pool width increased and edge sagging became prominent.

2.3 Cold spray

Cold spray (CS) is a solid-state manufacturing technique traditionally used for depositing metal powders (Fig. 4b). Compared to other refractory metals, Nb is relatively ductile and therefore compatible with CS. Unlike conventional thermal spray methods, CS does not require molten or semi-molten particles, which is useful given that Nb alloys possess both a high melting point and are susceptible to oxidation. Instead, CS relies on accelerating feedstocks in a supersonic stream of inert gas, causing them to deform upon impact with the substrate. The high-velocity impact shear deforms the particle into a "splat" [89]. This extreme deformation disrupts the oxide layer and facilitates both metallurgical bonding and mechanical interlocking with the substrate [90]. CS mitigates the problems of cracking and porosity during cooling from high temperatures inherent to fusion-based AM. However, it adds a new problem of introducing strain and porosity defects during splat deformation. In CS, the gas pressure, gas temperature, and particle size must all be tailored to the material to ensure high interparticle bonding and low porosity. Feedstock powder spheroidization is not always necessary and therefore simpler feedstock preparation methods, such as ball milling or attrition, can be used with lower cost than the GA and PS feedstocks needed for PBF [91].

As with other AM methods, O present in the carrier gas must be minimized to prevent embrittlement and the growth of surface oxides, which hurt interparticle bonding [92]. For example, three studies by Kumar et al. reported pure Nb manufactured via CS where the spray gas was air at 450 °C and 2 MPa [93–95]. In each study, they used a powder feedstock with an average diameter of 30 µm that was crushed, leading to a jagged and non-spherical morphology. The relative density of their samples was 99.7% as-deposited, which they were able to improve to > 99.9% by vacuum annealing at ≥ 1000 °C for 2 h. The relative density increased with increasing annealing temperature up to 1500 °C. They observed that the corrosion performance of the CS Nb was poor due to preferential corrosion at the boundaries between particle splats but was improved after vacuum annealing.

It is also worth noting preliminary evidence that the CS deposition of pure Nb has properties that may be suitable for superconducting radio frequency (SRF) cavities, but once again O contamination must be minimized by using an inert carrier gas [71, 95, 96]. Studies by Nault et al. [97] and Roper [98] demonstrated successful CS of pure Nb using He gas at 550–600 °C and 3.1–3.5 MPa instead of air; a study by Sotiropolous et al. [99] showed that N gas is also effective if a ceramic "shot-peening" powder is cold sprayed simultaneously to work-harden the Nb during CS to improve relative density. As demonstrated in these studies, high purity inert gas (He) can be used for critical components where O content must be minimized while cheaper gasses (air and N) can be used for less critical applications where gas cost is a greater concern.

3 Material properties

3.1 Mechanical properties

3.1.1 LPBF

Conventional manufacturing of pure Nb, such as casting followed by furnace cooling, results in a highly ductile material with a Vickers macrohardness (HV) of 81 HV, tensile yield strength (σ_y) of ~140 MPa, ultimate tensile strength (UTS) of ~200 MPa, and an elongation at break (ε_{ab}) of ~45% [13, 44]. Note that the overwhelming majority of studies in this review reported a Vickers microhardness, but any instances where conversions were necessary from other measurements followed the guidelines outlined in [100]. In the case of LPBF on pure Nb, Griemsmann et al. showed that a low VBR (0.4 mm^3/s) combined with a high VED (300 J/mm^3) resulted in a 99.9% relative density part (149 HV0.1, σ_y = 316 MPa, ε_{ab} = 12.6%) [49]. By contrast, Liu et al. showed that a lower VED (146 J/mm^3) and higher VBR (2.4 mm^3/s) achieved roughly the same density but with improved mechanical properties (300 HV0.1, σ_y = 553 MPa, ε_{ab} = 26%) [2]. A very low VED (100 J/mm^3) and a high VBR (1.8 mm^3/s) resulted in 98% density as well as diminished strength and ductility (σ_y = 490 MPa, ε_{ab} = 9%) [42]. The results of Liu et al. therefore demonstrated the best balance of strength and ductility, suggesting that 150 J/mm^3 is an optimal LPBF VED for pure Nb (Fig. 5). The uniquely high strength and ductility was attributed to the combination of high relative density with a high density of both low-angle grain boundaries and dislocations. Evidence from AM of stainless steels suggests that dense dislocation cell networks can improve both strength and ductility, thus more research into the effects of these structures in pure Nb is recommended [101–103].

Nb-521 and Nb-C103 processed via LPBF had similar strength characteristics to pure Nb. In the case of Nb-521, a low VED (87.5 J/mm^3) resulted in the highest relative density (99.2%), highest ductility and moderate tensile strength (σ_y = 395 MPa, ε_{ab} = 18%) [73], whereas a higher VED (143 J/mm^3) resulted in roughly the same density but with improved tensile strength at the expense of ductility (σ_y = 540 MPa, ε_{ab} = 8%) [40]. For Nb-C103, the same VED (121 J/mm^3) produced dissimilar results despite using the same LPBF instrument, the same commercially available feedstocks, and the same build layer thicknesses (0.03 mm). In the first case, Awasthi et al. produced a material with higher strength and lower ductility (σ_y = 540 MPa, ε_{ab} = 19%) [22], whereas DuMez et al. reported lower strength and higher ductility (σ_y = 447 MPa, ε_{ab} = 29%) [74]. The more ductile sample had a microstructure of slightly elongated grains parallel to the build direction (~ 63 µm diameter, 1.1:1 aspect ratio), whereas the stronger sample had smaller and highly elongated grains (~ 56 µm diameter, 5.6:1 aspect ratio) parallel to the build direction. The stronger sample also exhibited a high-density cellular network of dislocations, which, in conjunction with grain boundaries, impeded dislocation motion and likely enhanced the strength while maintaining relatively good ductility.

However, neither Dumez et al. nor Awasthi et al. fully reported their process parameters, making it difficult to assess which variables controlled the grain size and shape anisotropy. A VED of 169 J/mm^3 and 0.02 mm layer thickness used by Brizes et al. resulted in a much finer grain size (~ 22 µm diameter) and improved strength over the other LPBF Nb-C103 alloys at the cost of ductility (σ_y = 601 MPa, ε_{ab} = 15%) [66]. It is worth noting that Nb-Si alloys prepared by LPBF were significantly harder than the other Nb alloys in this review, due to the composite mixture of Nb_{ss} and Nb-Si phases [43].

The primary factors for improved strengthening from LPBF compared to casting are the LPBF microstructure as well as O embrittlement, which will be discussed later. The LPBF microstructure is characterized by having a fine grain size (45–80 µm for pure Nb [2, 42, 72], 12–80 µm for Nb-521 [24, 40, 73], and 22–63 µm for Nb-C103 [22, 66, 74]) and a high amount of retained thermal stress due to the rapid rate of cooling from melt (Fig. 6a**)**. The thermal stress results in a relatively high density of defect structures including dislocations, which combined with the high density of grain boundaries contribute to increased strength at the expense of ductility under well-understood theories of dislocation-based strengthening in metals [104, 105]. As mentioned previously, tuning the size of networks of dislocation cells may be one method to overcome this strength-ductility tradeoff.

PBF AM of BCC materials often results in a dominant < 001 > crystallographic texture along the build direction [22, 42]; however, alternative anisotropic texture orientations have been observed. For example, Chesetti et al. used a similar VBR, VED, and raster pattern to Liu et al. and both studies reported the development of < 111 > grain texture (the slip direction in BCC metals) aligned with the build direction. In contrast, Griemsmann et al., using a higher VED and lower VBR, did not develop < 111 > texture and reported lower σ_y and UTS along with an ε_{ab} that was between the values reported by Liu et al. and Chesetti et al. [49]. It is difficult to conclude the effect of anisotropic texture on the mechanical properties of Nb due to a lack of studies that systematically isolate texture from other variables, such as grain size and interstitial alloyants, and therefore it is worthy of further study (Table 1).

3.1.2 EPBF

EPBF of pure Nb resulted in a softer material with properties much closer to conventional processing. For example, Terrazas et al. reported a macrohardness (unreported applied load) of 82 HV (σ_y = 141 MPa, ε_{ab} = 34%) [44]. Notably,

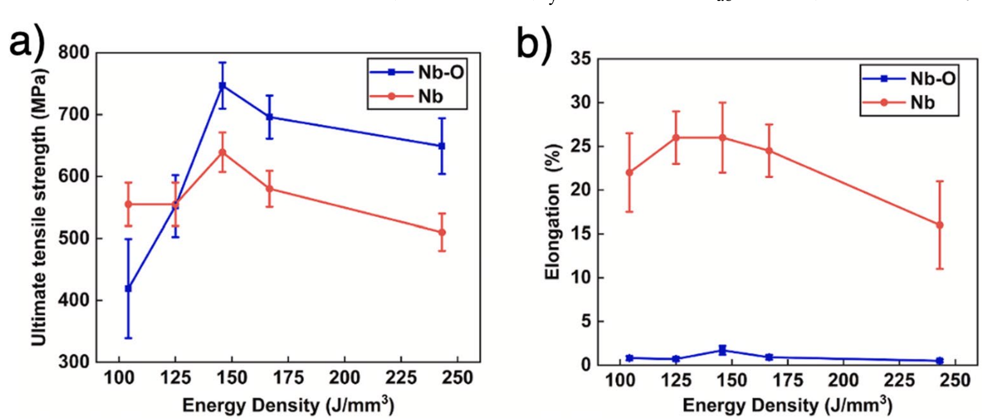

Fig. 5 The variation of **a** UTS and **b** ε_{ab} for LPBF of pure Nb and Nb-O, both from Liu et al. [2]. Reprinted with permission from Elsevier

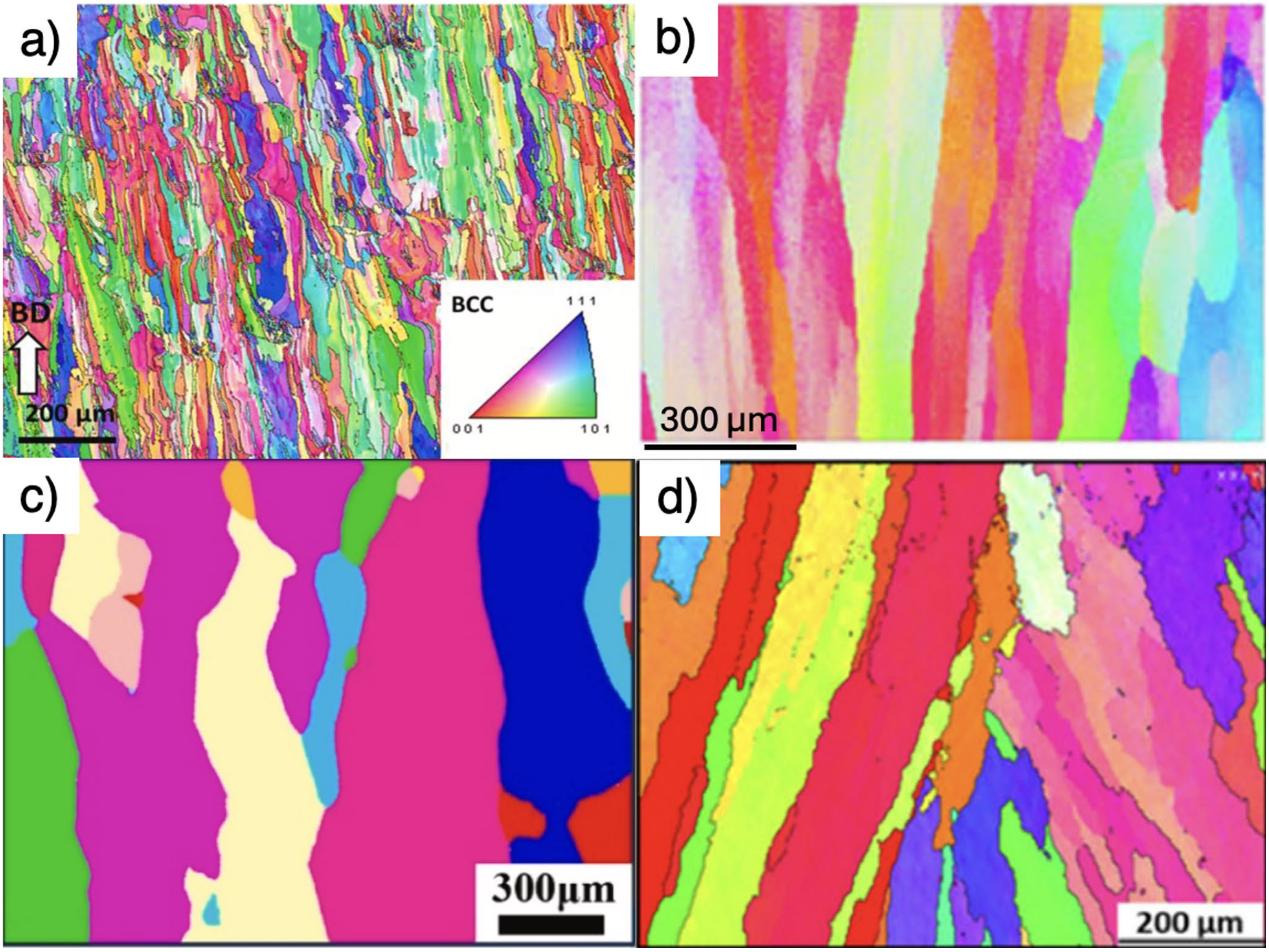

Fig. 6 The electron backscatter diffraction (EBSD) inverse pole figure (IPF) grain morphology of AM Nb alloys imaged with the build direction vertical: **a** LPBF Nb-C103 [22], **b** EPBF Nb-C103 [46], **c** LPDED pure Nb [70], **d** WADED Nb-1Zr [85]. Reprinted with permission (**a**) from Elsevier, (**b**) under CC BY 4.0 license from Springer [50], (**c**) from Elsevier, and (**d**) from Wiley

Table 1 Mechanical property ranges of available LPBF Nb alloys from tensile and hardness testing

Alloy	σ_y	UTS	ε_{ab}	HV	Refs.
Pure Nb	316–553	525–639	9–26	149–300	[42, 49, 71, 72]
Nb + O	703	747	1.7	N/A	[2]
Nb-521	395–540	623–629	8–18	220	[40, 73]
Nb-C103	486–601	447–632	15–29	193	[22, 66, 74]
Nb-Si	N/A	N/A	N/A	490–1410	[43]

N/A indicates that a value was not reported in the reviewed literature. HV reported following the guidelines of [100]

they reported no increase in O content between the precursor powder and the EBPF part and therefore O embrittlement was effectively mitigated. Under similar EPBF processing conditions and with the same powder precursor, Martinez et al. reported a microhardness (unreported applied load) of 94 HV for powder of uniform size and a hardness of 112 HV when the powder was sieved into a bimodal distribution [76]. In this case, they observed that the improved packing density of the bimodal powder improved the density of the manufactured Nb and therefore improved the hardness. As shown in Table 2, EPBF of Nb-C103 had improved strength over EPBF of pure Nb, albeit at the expense of ductility through solid solution strengthening [46].

Some less common Nb alloys have been processed via EPBF. As mentioned previously, Hankwitz et al. manufactured Nb-1Zr wt% (σ_y = 366.5 MPa, ε_{ab} = 23.6%) and Nb-10 W-1Zr-0.1 C wt% (σ_y = 301.0 MPa, ε_{ab} = 13.2%) [65]. Gao et al. processed Nb-Si-Ti with EPBF, producing a very hard material (700 HV0.5) with poor fracture toughness (~5 MPa$\cdot m^{1/2}$ for EPBF compared to ~14 MPa$\cdot m^{1/2}$ for as-cast) due to crack initiation at the boundary between the Nb-Ti and Nb_3Si phase regions [77, 106].

Microstructural differences of EPBF as compared to LPBF include a larger grain size (200 –250 µm for pure Nb [44, 76]), longer columnar grains parallel to the build direction, and lower retained thermal stress (Fig. 6b). The

Table 2 Mechanical property ranges of available EPBF Nb alloys from tensile and hardness testing

Alloy	σ_y	UTS	ε_{ab}	HV	Refs.
Pure Nb	141	225	34.3	82–112	[44, 76]
Nb-C103	247	354	25	N/A	[46]
Nb-1Zr	367	429	23.6	N/A	[65]
Nb-Si	N/A	N/A	N/A	700	[77]

N/A indicates that a value was not reported in the reviewed literature. HV reported following the guidelines of [100]

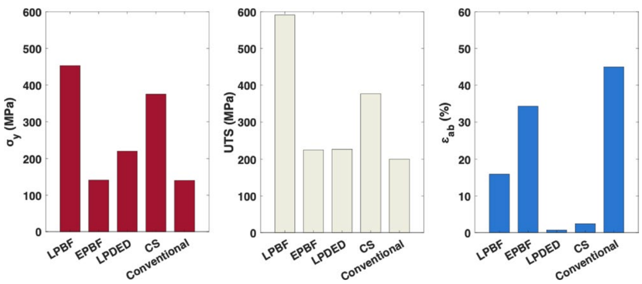

Fig. 7 A comparison of the average mechanical properties for the AM techniques used to fabricate pure Nb in this review. *Note* that data on WADED of pure Nb was not available

elevated ambient temperature of EPBF (610 –1100 °C preheated powder bed) reduces the severity of thermal cycling during the raster process compared to LPBF, slowing the cooling rate from melt, and keeping thermal stresses closer to those encountered during conventional processing. Therefore, one clear distinction between LPBF and EPBF is that EPBF produces mechanical properties closer to conventional processing, as clearly evidenced by the amount of strength exchanged for ductility. Comparing the inert gas used in LPBF to the vacuum condition used in EPBF, the vacuum prevents a significant amount of O from diffusing into the EPBF part. Additionally, the larger particle sizes used in EPBF make them less prone to oxidation during atomization of the feedstock.

3.1.3 LPDED

Of the limited studies using LPDED on Nb alloys, only Liu et al. reported tensile strength [70]. They showed that LPDED of pure Nb resulted in a relatively weak material with poor ductility (σ_y = 220 MPa, ε_{ab} = 0.7%) primarily due to large columnar grains (180 µm) parallel to the build direction (Fig. 6c). Despite the use of Ar shielding gas, oxygen embrittlement was also likely given the exceptionally low ductility (Fig. 7). The large grains showed intergranular cracking in the as-built condition that then led to brittle intergranular failure under tensile stress. One way they offset the large grain size of LPDED Nb was to introduce TiC nanoparticles into the powder feedstock up to 3 wt%. The introduction of TiC refined the grain size (112 µm), promoted equiaxed grains without intergranular cracking, and introduced α-Nb_2C precipitates, resulting in a drastic improvement in both strength and ductility (σ_y = 276 MPa, ε_{ab} = 17.8%). Given its higher affinity for oxidation compared to Nb, the addition of Ti likely also served as an oxygen absorber, mitigating Nb embrittlement [107]. Therefore, the introduction of precipitate-forming alloyants, like TiC, is an effective way to offset the negative impact of the large melt pool inherent to LPDED of Nb.

3.1.4 WADED

The only WADED studies reporting Nb alloy mechanical properties are from Islam et al. on Nb-1Zr wt% [41, 85]. As they varied the VED from 138 J/mm^3 (147 HV0.5, σ_y = 326 MPa, ε_{ab} = 25.2%) to 168 J/mm^3 (164 HV0.5, σ_y = 380 MPa, ε_{ab} = 24.5%), hardness increased, strength increased, and ductility remained roughly constant. This balance of tensile strength and ductility is quite similar to that of EPBF of Nb-1Zr. Like EPBF, WADED produced a large, columnar grain size but with dendrites branching off of the main columnar grains (Fig. 6d). They also reported a very low concentration of Nb oxides, which was due to a combination of the low surface area to volume ratio of the wire feedstock compared to powder, as well as the observed preferential oxidation of Zr into ZrO_2. Therefore, large grain size and low Nb oxide content contributed to the high ductility in both EPBF and WADED.

3.1.5 CS

Few studies to date have used CS for AM of Nb alloys, with only pure Nb being explored. Kumar et al. reported tensile strength for CS of pure Nb [93, 94]. They reported tensile values after annealing the as-sprayed materials at 1000–1500 °C for 2 h to improve the inter-particle bonding and density. Increasing the annealing temperature from 1000 °C (σ_y = 232 MPa, ε_{ab} = 0.7%) to 1500 °C (σ_y = 375 MPa, ε_{ab} = 2.4%) improved not only tensile strength but also elongation. Therefore, the heat treatment had the effect of closing pores, improving bonding between splats, and relieving the stress of plastic deformation [108]. The tensile properties are very similar to those observed by Liu et al. for LPDED of pure Nb, demonstrating that CS followed by annealing can achieve similar properties to a melt-based technique. However, the low ε_{ab} in the annealed state indicates that using air as the carrier gas introduced a high concentration of O into the CS Nb, preventing CS from achieving the combination of strength and ductility observed in EPBF and LPBF. Therefore, further study using N, He, or other inert gases is encouraged.

Roper investigated CS on pure Nb using He carrier gas instead of air and reported a compressive yield strength of 1.1 GPa [98]. Roper also applied a 1 kW (1.25 MW/m) constant laser heat source during the spray in a technique known as laser-assisted CS (LACS) to increase the surface temperature during deposition. Comparing the as-sprayed (300 HV0.5) and LACS (260 HV0.5) hardnesses, the extra heat from LACS relieved some of the residual stress from plastic deformation [109].

3.2 Oxygen embrittlement

One of the fundamental challenges of AM for Nb alloys is controlling the exceptional loss of ductility in exchange for strength due to O embrittlement. This limits the usefulness of Nb alloys in structural applications if ambient O is not minimized along the entire processing chain from feedstock to part. It is generally clear that, compared to conventional casting, LPBF improves the tensile strength of Nb at the expense of ductility. It was reported by Chesetti et al. that the presence of ≤ 1.3 at% interstitial O in pure Nb will cause strengthening as well as embrittlement hardening [42]. Interstitial N can have a similar effect, although at a less severe degree. They observed that interstitial O and N segregated to the grain boundaries in LPBF Nb but maintained a high enough concentration throughout the Nb matrix to impede dislocation motion and cause strengthening. Yang et al. reported strong coupling between crystal lattice vacancies and solute O, which stabilized the vacancies in the presence of screw dislocations and prevented their decomposition (Fig. 8a) [13]. Additionally, O-induced strengthening was observed by Liu et al. to come at the expense of ductility. ε_{ab} dropped from 26% for 0.05 wt% O down to 1.7% for 0.23 wt% O, with the corresponding σ_y increasing from 553 MPa to 703 MPa, respectively (Fig. 8b) [2]. Therefore, processes that minimize O uptake in the feedstock production and AM, such as EPBF and WADED, are best suited to producing Nb alloys with a combination of high ductility and strength.

3.3 Post processing

3.3.1 Annealing

One way to test the relative effect of O embrittlement versus other strengthening mechanisms based around dislocation motion, such as grain boundaries, crystalline defects, and solid solution strengthening, is to see whether the strengthening is reversible using a heat treatment to anneal out defects and increase grain size without changing the O content. For example, Hankwitz et al. achieved significant strengthening reversal in exchange for ductility on EBPF Nb-1Zr wt% by performing a vacuum anneal at 1200 °C for 4 h and 12 h [65]. As shown in Fig. 9, there was a smooth tradeoff between strength and ductility, suggesting that O embrittlement was not the primary strengthening mechanism in this case.

Philips et al. found a less conclusive tradeoff between strength and ductility in EPBF Nb-C103 by annealing under vacuum at 1500 °C for 4 h [46]. Comparing the as-fabricated (σ_y = 247 MPa, ε_{ab} = 25%) and annealed conditions (σ_y = 261 MPa, ε_{ab} = 28%), σ_y and ε_{ab} were both increased. This was likely due to the increased effect of solid-solution strengthening from the 10 wt% Hf present in Nb-C103, where the high-temperature annealing encouraged diffusion of Hf throughout the material that

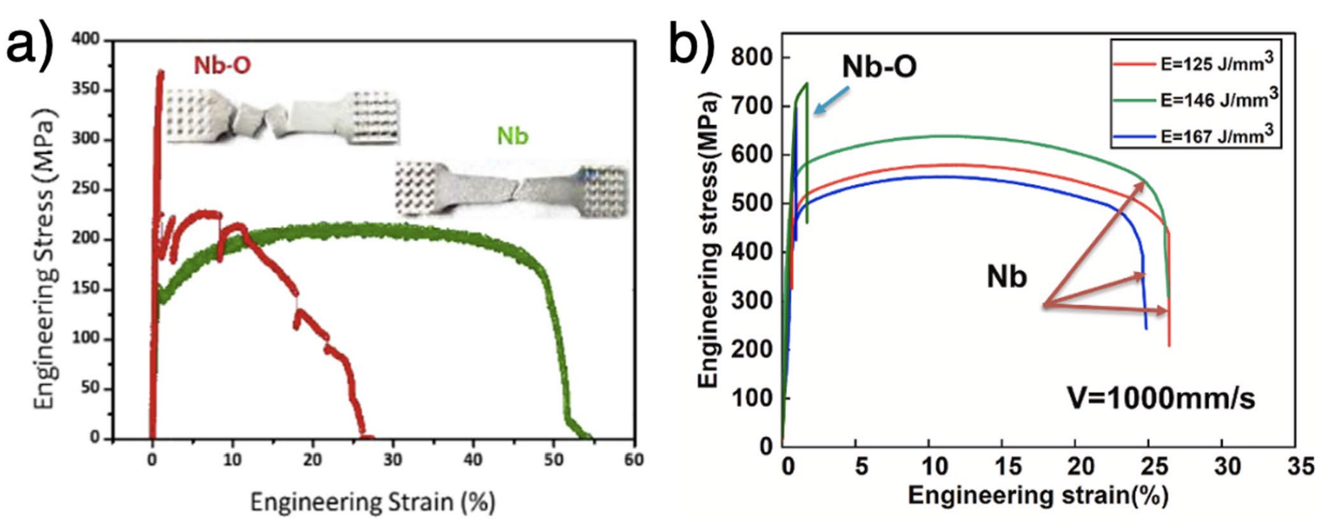

Fig. 8 Engineering stress-strain curves for pure Nb with and without the effect of O embrittlement from **a** Yang et al. with the tensile specimens shown as inset [13] and from **b** Liu et al. showing multiple values of VED [2]. Both reprinted with permission from Elsevier

may have remained segregated during EPBF. Results from Hankwitz et al. on EPBF of Nb-10 W-1Zr-0.1 C wt% support this hypothesis [65]. They observed that segregated clusters of W left behind from EPBF began to dissolve into the alloy matrix when annealed at 1200 °C for ≥ 4 h, improving both strength and ductility.

Therefore, while the strengthening due to dislocations is reversible through annealing, solid solution strengthening may actually be increased through annealing when alloyants like Hf and W are not well dispersed during AM. While annealing may have different effects depending on the composition of the Nb alloy in question, it is clearly possible to restore ductility after EPBF in some cases when O contamination is effectively mitigated. It is noteworthy that, despite the higher prevalence of O contamination, no studies on LPBF have explored whether strengthening was a result of O or other microstructural features, leaving this as an open question worthy of future exploration.

3.3.2 Hot isostatic pressing

Another common post-processing technique is hot isostatic pressing (HIP) at high pressures (> 100 MPa) to close voids and relax stress after AM. This is an effective solution to one of the fundamental challenges of AM for Nb alloys: it can remove defects caused by the severe thermal gradients formed when cooling from its high melting point.

For example, Brizes et al. performed HIP on LPBF Nb-C103 (1500 °C for 4 h in Ar) (Fig. 10) [66]. This had a drastic impact on the tensile strength, lowering σ_y by 44% but increasing ε_{ab} from 15% to 27%. HIP had a negligible effect on the measured density but increased the average grain size by a factor of 10 and eliminated almost all

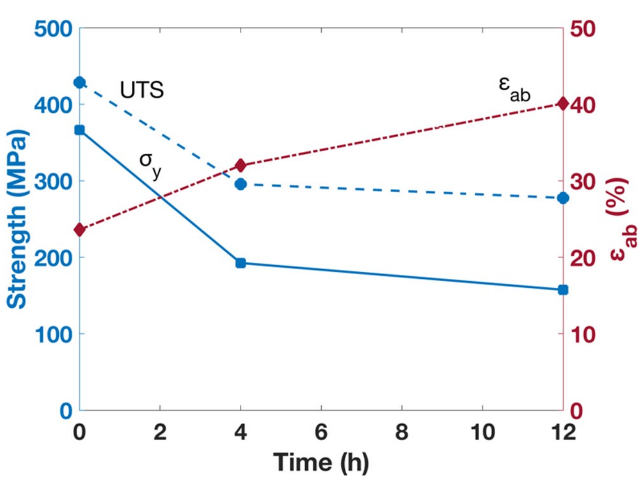

Fig. 9 The tradeoff between strength and ductility in EBPF Nb-1Zr wt% when annealed at 1200 °C. Figure drawn from data reported by Hankwitz et al. [65]

low-angle grain boundaries (< 15° misorientation). Similarly, Dumez et al. performed HIP on LPBF Nb-C103 (1593 °C for 2 h) [74]. In this case, the grain size increased by 150% and σ_y decreased by 31%, although ε_{ab} was observed to increase when the tensile load was applied parallel to the build direction and decrease when it was applied perpendicular to the build direction. This indicates that HIP is successful at relaxing the microstructure through grain growth, recrystallization, and dislocation motion and annihilation, but retains the material's anisotropy. In addition to the annealing in Sect. 3.3.1, Philips et al. performed HIP on EPBF Nb-C103 (1593 °C for 4 h) [46]. Interestingly, they observed a 14% increase in σ_y while ε_{ab} was unchanged and the relative density increased from 99.77% to 99.97%. They did not comment on changes to grain size, dislocation density, or O content, although prior work by Philips et al. has shown a ~ 100 ppm increase in O content in Nb-C103 powder subjected to HIP [10]. Thus, further study is needed to understand the full microstructural impact of HIP across the full range of Nb alloys and AM processes.

3.4 High-temperature oxidation resistance

Similar to their tendency to oxidize during AM, Nb alloys used in aerospace applications undergo high-temperature oxidation in air which can degrade their structural integrity. The oxide phases that tend to form on the surface at high-temperatures, Nb_2O_5 and NbO_5, are porous and do not form a passivating layer to prevent further oxidation [110]. Adding alloying elements that can form more compact oxide layers, such as Si, are a well-known strategy to improve the high-temperature resistance. Other strategies to mitigate high-temperature oxidation include coatings based on Si and Al, N-ion implantation, and forming the metastable $Nb_{12}O_{29}$ phase, which are beyond the scope of this review and readers should consult other recent studies for more information [74, 110–117].

A LPBF pure Nb and a LPBF Nb-W-C alloy were tested for high-temperature oxidation by Cardozo et al. [72]. Using thermogravimetric analysis (TGA), the samples were heated in air from room temperature to 1400 °C to observe their mass gain from oxidation. In the case of LPBF pure Nb, the onset of oxidation occurred at ~500 °C, which is the same as conventionally cast pure Nb [111]. In the LPBF Nb alloy with W-C, the onset of oxidation remained around ~500 °C, however, the rate of mass gain was lower compared to pure Nb up to ~1000 °C, beyond which the oxidation rates converged. Li et al. used LPDED to fabricate Nb-Ti-Si alloys with Zr, Cr, and Mo as additional alloyants and studied the oxidation behavior by annealing the alloys in air at 1250 °C [27]. The alloyants Zr, Cr, and Mo were found to improve

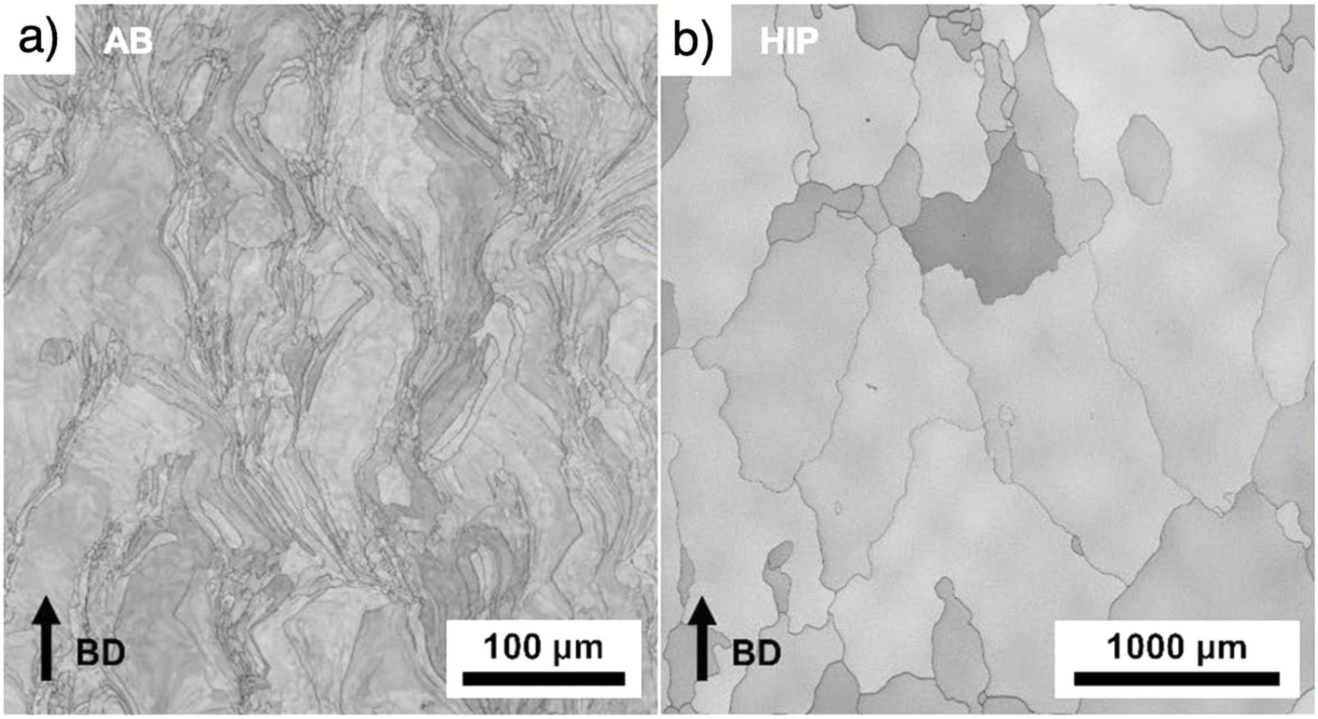

Fig. 10 EBSD band contrast images of LPBF Nb-C103 from Brizes et al. **a** as-built and **b** after HIP, showing the dramatic increase in grain size and loss of low-angle grain boundaries [66]. Reprinted with permission from Springer

the oxidation resistance following a descending effectiveness of Cr > Zr > Mo. The mass gain per unit surface area for $Nb_{63}Ti_{23}Si_{14}$ (130 mg/cm^2) dropped by a factor of 4 for $Nb_{53}Ti_{23}Si_{14}Cr_{10}$ (32 mg/cm^2), showing that substituting Cr for Nb can significantly improve the high-temperature oxidation resistance through the formation of a $CrNbO_4$ passivating layer. Similar studies on binary $Nb_{98} \times _2$ alloys produced by conventional processing has found that the descending effectiveness of alloying elements in preventing oxidation follows the trend V > Ti > Si > Cr > Al > W > Hf > Mo > Zr at 350 °C, indicating that oxidation resistance may vary depending on the manufacturing method and the other elements present in the alloy [118].

3.5 Thermal stability

Creep resistance is an important extrinsic property of Nb alloys for sustained structural performance under extreme thermal and mechanical loads. It describes their suitability as replacements for Ni-based superalloys in high-temperature turbine blades [119], hypersonic vehicle leading edges, control surfaces, and engine inlets [120]. Unfortunately, existing data on creep resistance of conventionally processed Nb alloys is sparse, and the literature does not yet cover those that are additively manufactured. According to Bowling et al., most conventionally manufactured Nb alloys exhibit creep resistance dominated by a solute drag mechanism (i.e. Class 1 creep), where alloyants Hf and Zr improve creep resistance [79]. Furthermore, a high annealing temperature is generally correlated with improved creep resistance, due in part to the formation of precipitates, although the undetermined overall mechanism requires further study.

Despite the gaps in reported literature, there is a small but growing body of work on how the tensile properties of some AM Nb alloys vary at high-temperature. For example, Sun et al. performed tensile testing on LPBF Nb-521 at room temperature and at 1200 °C in a vacuum environment to minimize oxidation [40]. Room temperature strength (σ_y = 540 MPa, ε_{ab} = 8%) diminished significantly at 1200 °C but ductility slightly improved (σ_y = 200 MPa, ε_{ab} = 10%). However, the LPBF sample maintained a higher absolute strength than conventional hot-rolled and annealed Nb-521 reported by Bukhanovsky et al. at room temperature (σ_y = 320 MPa, ε_{ab} = 29%) and 1200 °C (σ_y = 117 MPa, ε_{ab} = 44%) [121]. Despite this, the LPBF Nb-521 alloy had roughly the same relative loss of strength as conventional processing but without a significant improvement in ductility. The low improvement in LPBF Nb-521 ductility was largely attributable to the high density of ZrO_2 precipitates, dislocations, and elevated porosity as compared to the hot-rolled sample.

A comparison of the change in tensile properties with temperature of Nb-C103 for different processing techniques is shown in Fig. 11. The tradeoff between strength and ductility is quite similar to Nb-521, where increasing

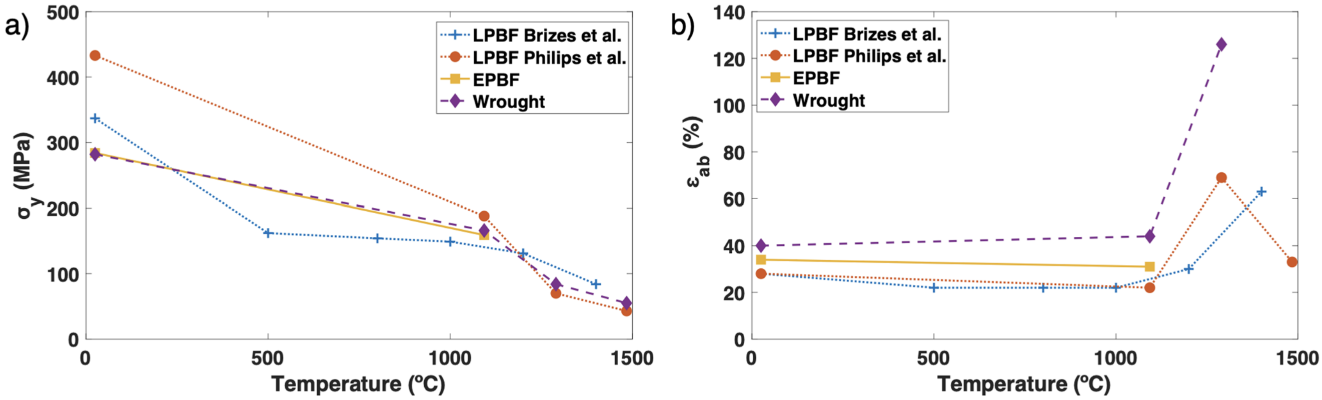

Fig. 11 The change in Nb-C103 tensile strength and elongation with temperature. LPBF samples were annealed at > 1300 °C for ≥ 1 h prior to tensile testing. Drawn with data from Philips et al. [10] and Brizes et al. [66]

temperature lowers strength without a meaningful increase in ductility up to ~ 1200 °C. However, above 1200 °C, there is a dramatic recovery in ductility in both the LPBF and wrought samples due to recrystallization, which begins around 1000 °C in Nb-C103 [66].

Given the applicability of Nb alloys to structural materials in harsh environments, further investigation of the strength and microstructural evolution at moderate (500–1000 °C) and high (> 1000 °C) temperatures is needed across all the AM processes in this review. Specifically, the dominant mechanisms affecting creep, strength, and ductility, as well as differences among the different Nb alloys and intermetallics, must be studied to isolate whether high-temperature properties are extrinsic, as a result of the AM process, or intrinsic to the specific Nb material composition (Fig. 7).

4 Physical simulations and data analytics

4.1 Physical simulations

Within the context of AM, physical simulations can isolate process variables and explore their effects across multiple time and length scales. Generally, physical simulations include first-principles (FP) calculations, phase-field (PF) modeling, and finite-element methods (FEM). FP calculations provide insight into the nano-scale quantum physical phenomena relevant to material behavior. PF modeling is well suited for capturing micro-scale processes such as diffusion and liquid-solid phase transformations. FEMs are effective for modeling thermal gradients, residual stresses, and mechanical deformation during manufacturing and/or testing at the macroscale. A summary map is shown in Table 3 to illustrate the various scales and applications addressed by different simulation methods.

Table 3 Summary mapping of simulation methods to AM outcomes for Nb alloys with concepts adapted from [115]

Scale	Model	Mechanism	AM applications
Nano	FP	Electrons/Atoms	Crystal phases, Thermal stability, Alloyants, Oxidation, Crystal defects
Micro	PF	Microstructure/Interfaces	Defects, Grain size, Porosity, Melt Pool
Macro	FEM	Heat flow/Bulk material	Distortion, Strength, Residual stress

To date, few studies have applied modeling techniques to Nb alloys, and even fewer have reported modeling Nb alloys for AM. Yet, while some examples in this section may not specifically focus on Nb alloys, the modeling methods are highlighted for their potential to be translated to the Nb material system to solve aforementioned challenges of efficient AM process selection, composition selection for oxidation resistance, and minimization of AM defects.

4.1.1 First-principles simulations

At the smallest scales, FP calculations of the electronic and atomic structures have been used to model the phase stability, crystal structure, elastic properties, and oxidation resistance of Nb alloys. For instance, Reynolds et al. carried out density functional theory (DFT) to investigate the interactions between interstitial O atoms in Nb-X-O materials (X = Al, Cr, Hf, Mo, Re, Ru, Sc, Si, Ta, Ti, V, W, Y, and Zr) [122]. The variation of binding energy strength between the X and O atoms was largely ascribed to a geometric mismatch effect that can be rationalized through atomic attributes, making it straightforward to choose Nb alloyants for improved oxidization resistance. A subset of FP modeling, molecular dynamics (MD) has been applied to pure Nb in multiple studies. For instance, Jain et al. used MD to model the hyper-local heat transfer of a modeled cylindrical supercell of BCC Nb atoms using the embedded atom method (EAM) interatomic potential [123]. They divided the supercell into three different cylindrical layers, from inside to out radially, and applied heating and cooling to the different layers at a rate of 1 °C/ps and 5 °C/ps, respectively, to observe atomic-level variations in melt behavior. Rapid cooling from high-temperature produced amorphous and distorted BCC clusters in the supercell prior to stabilization of the BCC phase. Therefore, MD can help predict the atomic-level aspects of solidification from melt needed to inform larger scale modeling like FEM.

Other examples of MD modeling less directly applicable to AM include modeling of crack tip propagation [124] and point defects like vacancies [125–127] in single crystal pure Nb, which can aid in predicting oxidation behavior in Nb. Other studies have developed custom empirical inter-atomic potentials for Nb alloys which were fit into DFT-calculated materials properties. For example, Yang and Qi employed a strategy to create a modified EAM potential that was able to reproduce multiple mechanical properties of Nb, including ideal shear strength and ductility, accurate dislocation properties, and phonon spectrum in agreement with DFT calculations [128]. By considering the motion of crystalline defects, rather than the perfect crystal lattices of DFT, MEAM bridges the gap to the micro-scale and allows for more realistic models of Nb alloy mechanical properties under applied stress. Therefore, there is a small but growing body of FP work on Nb alloys to aid in alloy selection, with specific attention to oxidation resistance, and predict material properties for efficient multi-scale modeling of AM.

CALPHAD modeling establishes the relationships between chemical composition, material properties, and phase stability, enabling accelerated optimization of composition in AM of Nb alloys, especially in high-temperature applications [119]. Bowling et al. conducted a comprehensive CALPHAD study of common Nb alloys and validated modeled properties against experimental results [80]. They reported good agreement between CALPHAD predictions and measurements for specific heat capacity and coefficient of thermal expansion. Additionally, they compiled experimental data and developed empirical models for elastic modulus and thermal conductivity. Together, these thermophysical properties serve as essential inputs for higher scale models like FEM to predict AM process outcomes. However, standard CALPHAD databases may not explicitly account for elevated oxygen concentrations, which are common in fusion-based AM processes like LPBF and LPDED; future validation should determine whether existing models remain accurate for oxygen contaminated AM Nb alloys or require modifications to account for interstitial oxygen effects.

4.1.2 Phase-field modeling

The material properties of additively manufactured alloys are governed by their resulting microstructure, which evolves during the AM process [2, 3, 22, 129]. However, the characteristic length scale of most microstructural features (~10 μm) is far beyond the capability of FP calculations (~1 nm), even using the most powerful supercomputers. PF offers a micro-scale simulation approach for capturing microstructural evolution, by incorporating thermodynamic driving forces such as interfacial energy and different transport phenomena, such as heat conduction and diffusion [130, 131]. It significantly reduces the degrees of freedom, and therefore computational complexity, by treating the microstructure evolution as variations of order parameters.

In the most relevant study of PF modeling applied to AM of Nb alloys, Prabhune et al. applied the volume of fluid (VOF) method of computational fluid dynamics (CFD) to model LPDED of Nb-C103 [87]. In this study, they modeled the interfacial interactions between the solid powder particles, molten deposit, and the solid interface along with the associated heat flows to reasonably predict the height and width of one track of LPDED at different laser power inputs (Fig. 12). The ability to accurately predict the geometry of the LPDED track rapidly expedited the selection of a Nb alloy processing window (e.g. laser power, scan speed, raster geometry) that was free of lack of fusion and keyhole defects.

While not a true Nb-majority alloy, Ti-Nb processed with AM has been explored with PF modeling to predict the heat flow within the melt pool and the resulting microstructure. Fallah et al. used PF modeling of the solid-liquid interface during LPDED of Ti-30Nb at% to accurately predict the dendrite arm tip radius and dendrite spacing as it varied along the build direction, aligning well with experimental observation of a dendritic spacing minimum distance near the midpoint of the build height [132]. Likewise, Cheng et al. applied CFD PF modeling to LPBF of Ti-25Nb at%, modeling the cooling rate in a bulk solid model as well as in a powder bed model, revealing a deviation of cooling rate between the two of up to 27% [133]. This clearly revealed the importance of incorporating the powder bed characteristics when predicting heat flow during LPBF. Perhaps most importantly, their model allowed them to observe when the local cooling rate would lead to dendritic, cellular, or planar grain morphologies, a key factor in selecting the LPBF processing parameters.

Similar research on other material systems is translatable to Nb alloys and shows the potential for PF modeling in AM. For example, Zhang et al. used PF to analyze the role of powder particles in LPBF porosity and density [134]. Their results indicated that smaller particles mixed

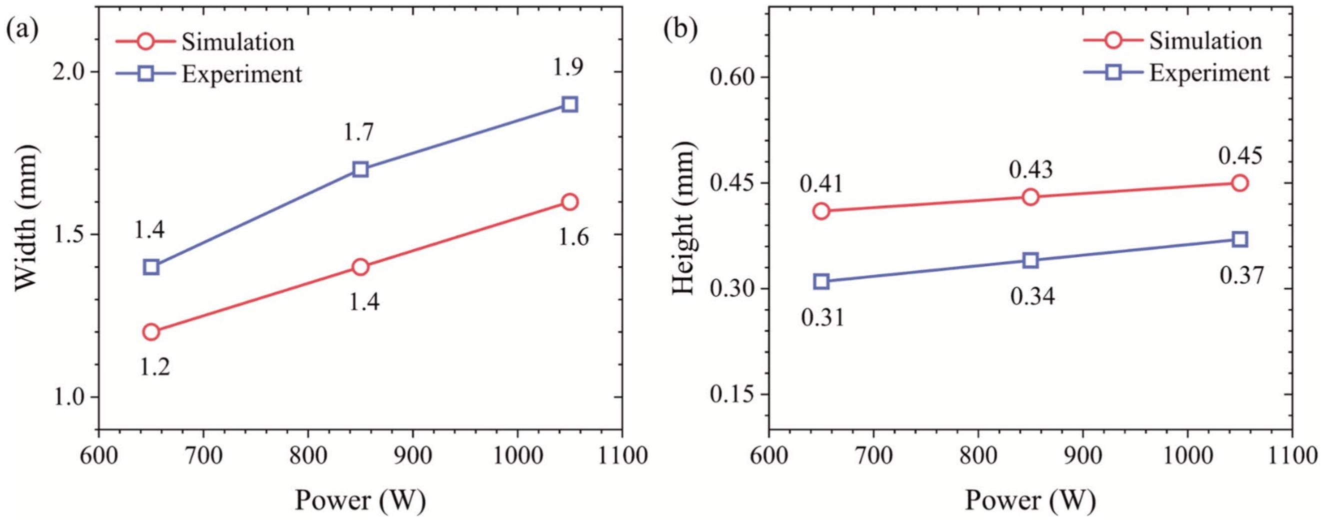

Fig. 12 CFD simulation of how Nb-C103 LPDED track geometry varies with laser power in terms of **a** width and **b** height as compared to experimental validation. Reprinted from [87] under CC BY 4.0 license from Elsevier [50]

with larger particles contributed to higher density because it improved packing during spreading and aided the sintering coalescence between particles. This agrees well with the effects of a bimodal powder size distribution in EPBF observed by Martinez et al. in Sect. 3.1.2 [76].

Thus, while PFs have successfully reproduced experimental AM observations in other material systems, they have only recently been applied to the AM of Nb-majority alloys. Given the high cooling rate from melt and prevalence of porosity in Nb alloys made with AM, PF should be further explored as a line of inquiry to aid in processing window selection and porosity defect control.

4.1.3 Finite-element methods

At the macro-scale, FEMs provide physical insights into how temperature distribution and residual stresses develop during an AM process. In FEM, the behavior of each element at each time step is governed by physical principles describing mechanical and thermal responses, typically represented by constitutive models and heat flow equations. Input parameters generally include part geometry, material parameters (e.g. density, thermal conductivity, Poisson's ratio, etc.), meshing schemes (e.g. types of elements and meshing strategy), as well as specifications of heat models and boundary/initial conditions that are necessary to determine evolution of the physical properties with time [135].

Jain et al. used FEM to model the heat flow during electron beam welding of pure Nb [53]. This enabled them to predict the melt pool geometry and heat flow into the surrounding solid material over time, as well as predict the maximum temperature within the melt pool. While this model assumed an electron beam encountering a solid material, rather than powder as in EPBF, it is one of the few examples of how to apply FEM modeling to EPBF of Nb. Islam et al., whose WADED study was reviewed in Sect. 3.1.4, applied FEM to generate a calibrated and validated stress-strain model of Nb-1Zr wt% by incorporating crystal plasticity (CP) into the model [41]. Starting with a model of predicted parameters from the as-built WADED microstructure, they iteratively adjusted parameters until the modeled stress-strain response approached the experimental calibration, resulting in a model that matched the UTS and σ_y of the validation data within 3% error. However, they noted that because the model relied on periodic boundary conditions and did not incorporate sub-grain features like dendrites, it could not accurately model the strain localization observed in experimental plastic deformation due to the inhomogeneous residual thermal stresses in WAAM.

Therefore, FEM stands to simplify the process optimization of fusion-based AM for parts requiring high geometric precision and minimize the loss of time and costly raw materials in trial-and-error experimentation.

4.2 Multi-scale multi-physics modeling

Due to the complexity of AM processes, multi-scale and multi-physics simulations are necessary to describe the physical phenomena occurring across various scales: from DFT, to PF, to FEM. While the aforementioned combination of MD and FEM for electron beam welding of pure Nb by Jain et al. comes close, no truly multi-scale models have yet been reported for AM of Nb alloys. A closely related study by Zhang et al. explored a multi-scale combination of PF and FEM thermal models with a CP mechanical model [136] in LPBF, but with a Ti-21Nb at% alloy. In their workflow, the FEM thermal modeling stablished the cooling dynamics from melt, which then was used as the input for the PF modeling of dendritic and cellular microstructures based on different LPBF process parameters (laser power and raster speed). The output microstructures were then fed into the CP mechanical model to predict the mechanical properties of strength and hardness and showed reasonable agreement with experimental validation. Another study by Ghosh et al. followed the same general workflow to model LPBF of Ni-5Nb wt%, utilizing FEM to model the heat flow during cooling and then feeding this into a PF model to simulate the dendritic microstructure and concentration distribution of the Nb alloyant [137]. These predictions can be used to inform any post-processing needed after AM to achieve a homogeneous microstructures and distribution of alloyant elements.

Despite the lack of multi-scale modeling studies on Nb alloys, a materials-agnostic example of how multi-scale models can be translated to Nb alloys, based on multi-scale simulations on Ti alloys developed by Yan et al., is outlined in Fig. 13 [138]. At the nano-scale, a FP model was developed to simulate electron-atom collisions from an electron beam heat source. At the micro-scale, PF methods were used to model the grain growth and subsequent coarsening within one molten pool track. Macro-scale FEM models were focused on predicting the residual stresses and temperature gradients for repeating molten pool track layers at larger time and length scales. Combined into one layered model across scales, this framework was able to inform the powder selection and optimization of AM instrument parameters. Thus, translating these principles would allow for the rapid optimization of instrument parameters for new Nb alloy compositions while minimizing trial and error.

4.3 Data analytics and machine learning

As has been reported throughout this review, there is a critical lack of comprehensive study of AM processing of Nb alloys, especially in terms of data analytics and ML, and thus a lack of evidence to analyze and draw broad conclusions from. Therefore, this section reviews the sparse reports of applying data analytics to Nb alloys as well as reviews modeling of AM for similar alloys and how these

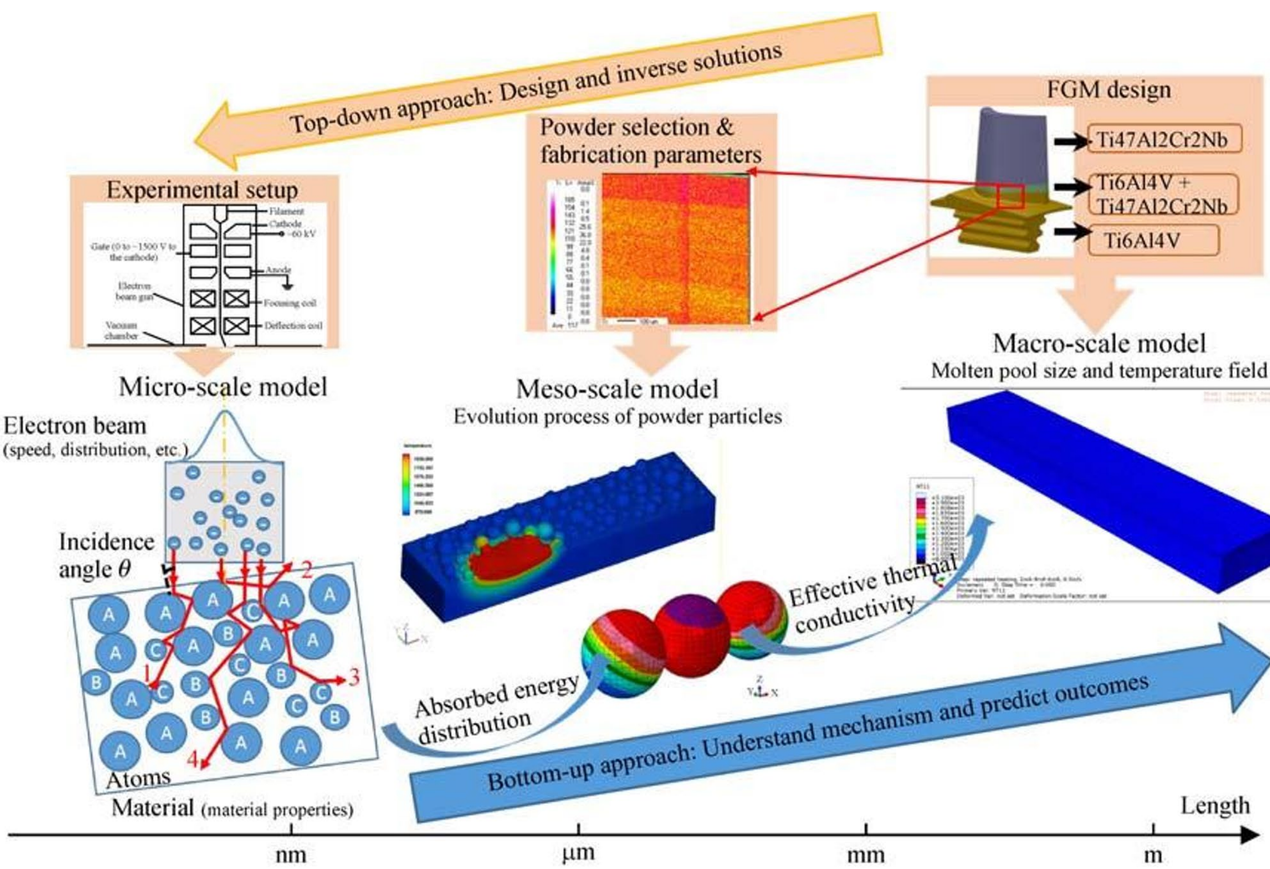

Fig. 13 Multi-scale simulation framework to link process, structures and properties. Reprinted from [138] under CC BY 4.0 license from Springer [50]

prototypical studies show promise for being applied to AM of Nb alloys.

4.3.1 ML for Nb alloys

While computational modeling has shown aptitude for overcoming some of the challenges inherent to AM of well-studied Nb alloys, such as compositional design for oxidation resistance and optimizing mechanical properties, ML can help expedite material selection of novel Nb alloys from a large space of candidate compositions.

In the most relevant example regarding mechanical properties, Mohanty et al. utilized a gradient boost regressor ML model of various Nb (plus any of the 14 common alloyants) alloy compositions, trained on existing experimental data on thermal and mechanical properties, to predict UTS and σ_y variation with temperature for different alloyant combinations [139]. Their Bayesian optimization method efficiently scaled down their alloy search space from ~ 1.6×10^6 unique quaternary alloy compositions and ~ 60×10^6 unique quinary alloy compositions to a shortlist of 7 candidates with optimal high temperature strength performance. In a similar study, Xiong et al. used a "gray wolf optimization-extreme learning machine" ML model to optimize Nb-521 composition when alloying with low levels of Sc and Y [140]. These elements, though costly in their raw materials, can provide useful precipitate or solid-solution strengthening. Thus, their ML model enabled them to predict σ_y and ε_{ab} for various combinations of Sc and Y in the Nb-521 matrix with relative deviation from experimental validation values of ~ 2% for σ_y and ~ 27% for ε_{ab}. This study suggested that ε_{ab} is more sensitive to minor changes in microstructure and was therefore more challenging for the ML model to accurately predict than σ_y. One way to improve the prediction of ε_{ab} is to train ML models on entire stress-strain curves, rather than discrete outputs like UTS and σ_y, as demonstrated by Wei et al. on Nb-W-Mo-Zr-Ta-Hf alloys [141]. They used a multimodal-transformer ML model trained on stress-strain curves of various compositions within the alloy system to predict an optimal composition. This data was combined with physics-based elemental alloy descriptors, like atomic radius and enthalpy of mixing, and a text description of the alloy processing method to account for variables like heat treatment or plastic deformation. Their model indicated that the composition Nb-6 W-2Mo-1Zr-6Ta-1.5Hf-0.05–0.2 N wt% should outperform Nb-521, and their experimental validation showed a relative 35% improvement in UTS over Nb-521 while keeping $\varepsilon_{ab} = 28\%$.

Less attention has been paid to applying ML to optimizing the oxidation behavior of Nb alloys specifically, however recent results on Nb-containing refractory high entropy alloys (RHEAs) can shed light on how to apply ML to this problem. Dong et al. used an extreme gradient boosting ML model to predict oxide weight gain for various combinations of Nb-Ti-Zr RHEAs alloyed with Cr, Al, V, Ta, Mo, Si, W, and/or Hf [142]. This model suitably predicted the relative oxidation rate at 1200 °C and identified that adding Cr, Al, and Si as alloyants to Nb-Ti-Zr slowed oxidation. However, using this and other forms of ML models like random forest regression for predicting corrosion behavior can result in a "black-box" understanding of the problem. Therefore, Shapley algorithm analysis was required in this and similar studies [143] to uncover the statistical importance of an input (e.g. alloyant amount) on an optimized output (e.g. oxidation resistance) and ensure the model aligned with known physical principles of corrosion behavior.

4.3.2 ML for process optimization

ML models have been developed to optimize the AM processes of many alloys, spanning applications from defect detection to real-time process control, thereby reducing reliance on skilled operator input. The emergence of computer vision algorithms has advanced the capabilities of AM in-situ monitoring and defect detection. For instance, Scime and Beuth used computer vision algorithms to identify various defects in LPBF (Fig. 14), allowing operators to automatically locate a build failure [144]. The algorithms were proven to be robust and versatile on builds of stainless steels, Inconel 718, Ti-6Al-4 V and AlSi10Mg, suggesting they can be readily translated to Nb alloys. Jin et al. used a ML model to enable iterative and adaptive optimization for a DED process [145]. Real-time monitoring and optimization were enabled by computer vision and the fast response of the ML algorithms. The technique was found to achieve 98% prediction accuracy on the printed part status quality, and it responded much faster to defect corrections compared to expert human operators. These advances in automatic flaw detection could be adapted to the processing of Nb alloys, offering a valuable use case for preemptively detecting flaws in high-performance applications like aerospace and power plants. By halting flawed builds early, these techniques help conserve both manufacturing time as well as expensive raw materials. While some aspects of ML flaw analysis may readily translate, such as identifying large pores or lack of fusion defects, adaptations will require training ML models on the unique flaw characteristics of Nb alloys mentioned in Sects. 2 and 3, such as evidence of oxidation and porosity caused by the increased cooling rate from melt.

Liu et al. used ML to efficiently optimize the LPBF process parameter window for AlSi10Mg samples [146]. By

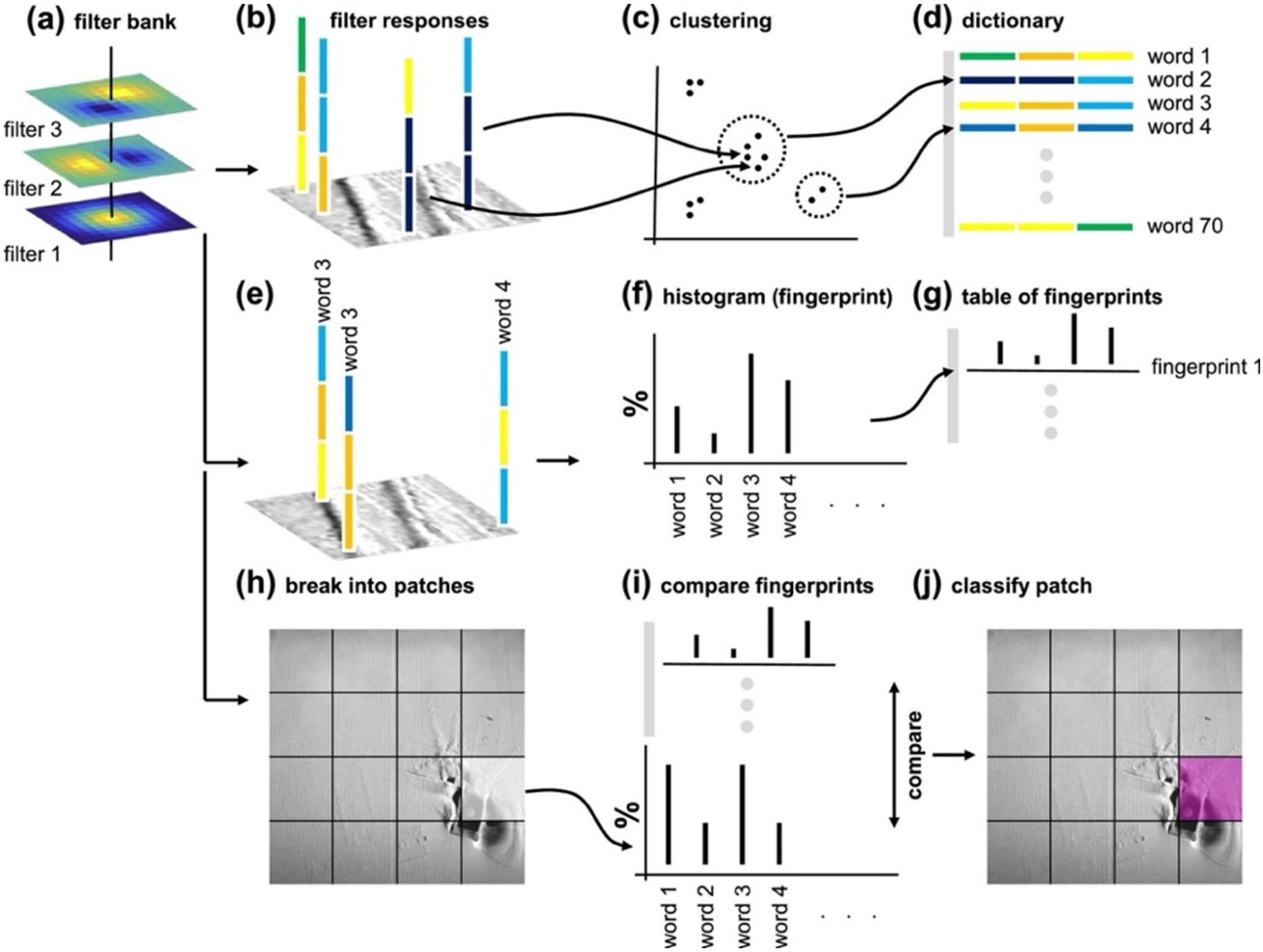

Fig. 14 An example flow chart using ML to identify various defects in LPBF. Reprinted from [144] with permission from Elsevier

fixing hatching space and layer thickness, the ML model generated a map of scan speed and laser power that accurately predicted the process parameters leading to ≥ 99% density (Fig. 15). Moreover, using computer vision of electron microscopy images, they were able to extract quantifiable differences in microstructure that could explain differences in strength between different AM AlSi10Mg samples. Therefore, alone or in conjunction with multi-scale modeling, these ML techniques can be used to rapidly expedite AM process window selection for new Nb alloys, thus saving time and costly raw materials. Furthermore, ML microstructural image processing techniques can supplement human expertise in explaining complex process-structure-property relationships, which is especially valuable considering the lack of comprehensive AM data for Nb alloys. However, researchers may benefit from keeping the variable space limited to only the most important variables in terms of minimizing computation as well as simplifying experimental validation.

4.3.3 ML-enabled multi-scale simulations

ML simulations aim to establish a cohesive link between input AM process parameters, microstructure evolution, and materials properties outputs. While multi-scale simulations in AM can apply separate computational models across different length and time scales, challenges remain due to the high computational cost and difficulty in combining models of differing scales. ML can produce reduced-order models, which mimic the behavior of complex systems with lower computational demands. For instance, Ma et al. developed an integrated ML/PF model for Inconel 718 to predict the microstructure at various cooling rates and temperature gradients in LPBF [147]. The ML was trained on PF microstructural evolution simulations, and the PF results were validated against experimental LPBF EBSD images. Similarly, Boillat et al. combined FEM and ML to simulate the laser melting process of Ti alloys by computing the temperature, specific enthalpy, density, and sintering potential of the powder [148].

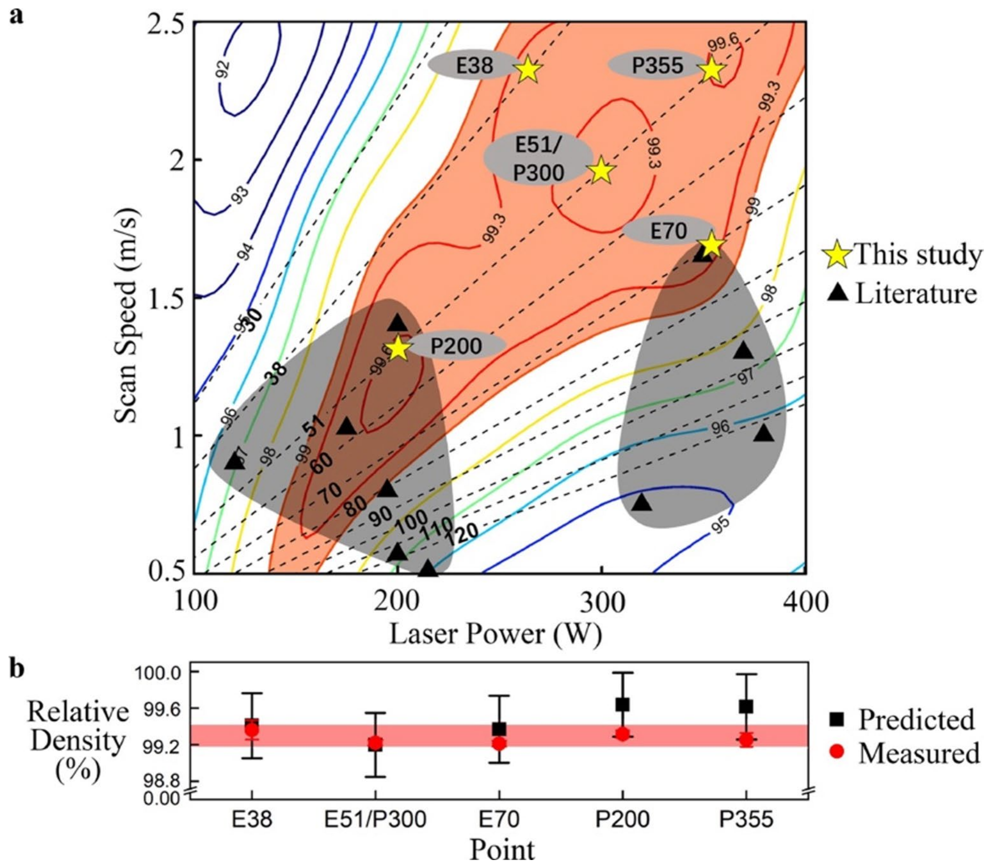

Fig. 15 Process map as a function of laser power and scan speed from Liu et al. Orange regions were identified as the process conditions where > 99% relative density could be achieved. Yellow stars were parameter sets chosen for experimental validation. Figure reprinted from [146] with permission from Elsevier

To reduce the need for well-described training data, which is currently lacking for AM of Nb alloys, fundamental physical equations (such as the differential equations governing heat flow) can be incorporated into ML models. For instance, Zhu et al. used a physics-informed neural network (PINN) to predict Inconel 625 laser melt pool dynamics and temperature gradients without needing an extensively large training dataset [149]. Similarly, Ren et al. demonstrated the use of a PINN trained on FEM data to map out temperature gradients in laser DED [150]. These methods are broadly materials agnostic and readily translatable to any metal system. Therefore, given the relatively small amount of existing training data on AM of Nb alloys, the PINN framework makes it possible to apply ML to predict certain simple AM properties like melt pool dynamics. However, researchers should exercise caution when using sparse training data to predict more complex multi-scale properties.

To overcome the challenge of sparse training data, recent efforts have focused on integrating experimental data with simulated data to generate comprehensive datasets that neither approach could provide alone. The integrated strategy also makes real-time process monitoring and control in AM more practical, transforming data collected during AM into a comprehensive dataset, known as a "digital-twin", that can accurately describe the properties of a real AM part. For example, Du et al. combined LPBF experiments, mechanistic modeling, and PINNs to create a digital twin to more reliably predict defects (Fig. 16) [151]. Likewise, Gunasegaram et al. developed a PINN workflow for digital twins in PBF and DED to expedite anomaly detection and process optimization [54]. Thus, similar to PINNs, digital twins for AM of Nb alloys can be improved by supplementing the modest amount of existing experimental data with simulated data, making process optimization far more efficient.

5 Conclusions

5.1 Summary

This review surveys AM of pure Nb and its alloys, including Nb-C103, Nb-531 and Nb-Si, by LPBF, EPBF, LPDED, WADED, and CS. Further, computational materials science and ML-assisted discovery are highlighted as powerful tools for accelerating the development of Nb alloys tailored for AM. It is evident that the mechanical properties of AM Nb alloys can approach those of conventionally manufactured counterparts. Comparing amongst AM techniques:

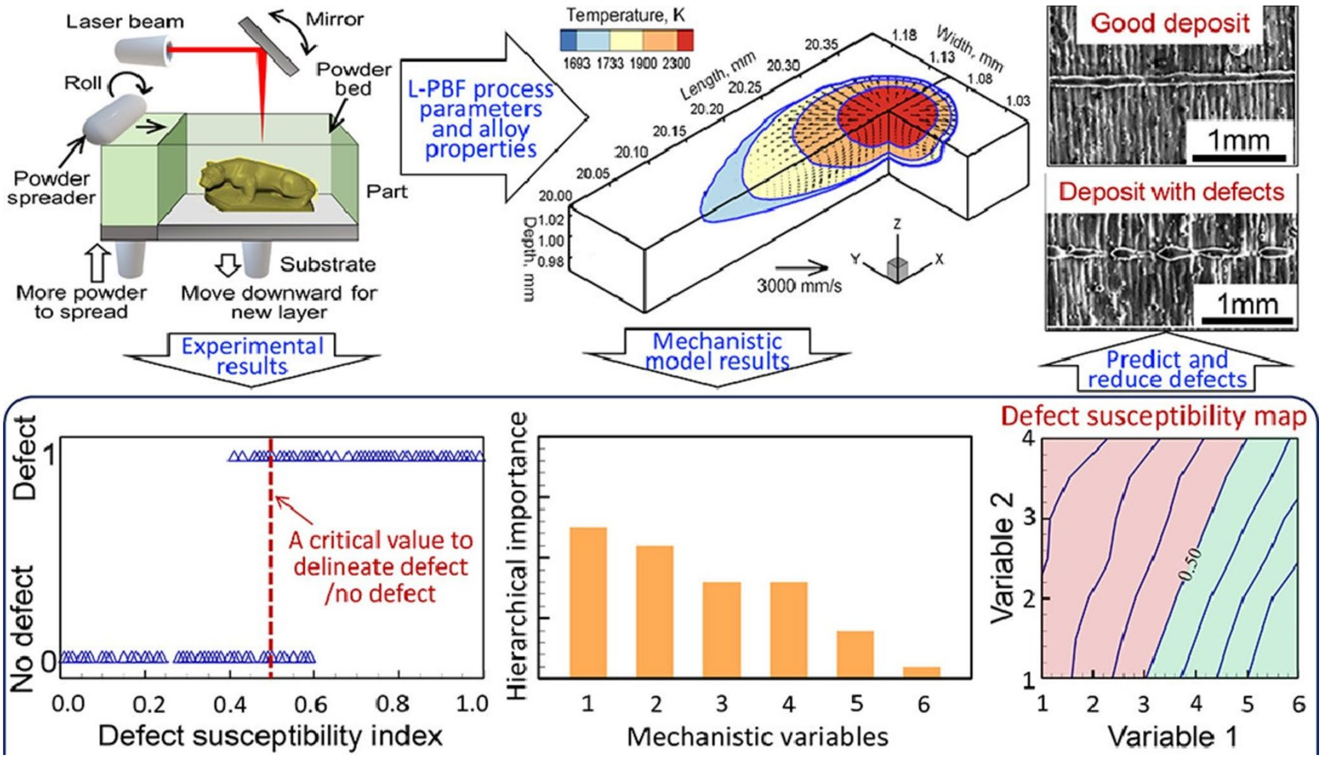

Fig. 16 A schematic of the approach by Du et al. combining experiments, mechanistic models, and physics-informed ML to predict defects in LPBF. Reprinted from [151] with permission from Elsevier

Fig. 17 A comparison of strength and ductility across the range of Nb alloys and AM methods covered in this review. Properties are given as-manufactured unless otherwise stated

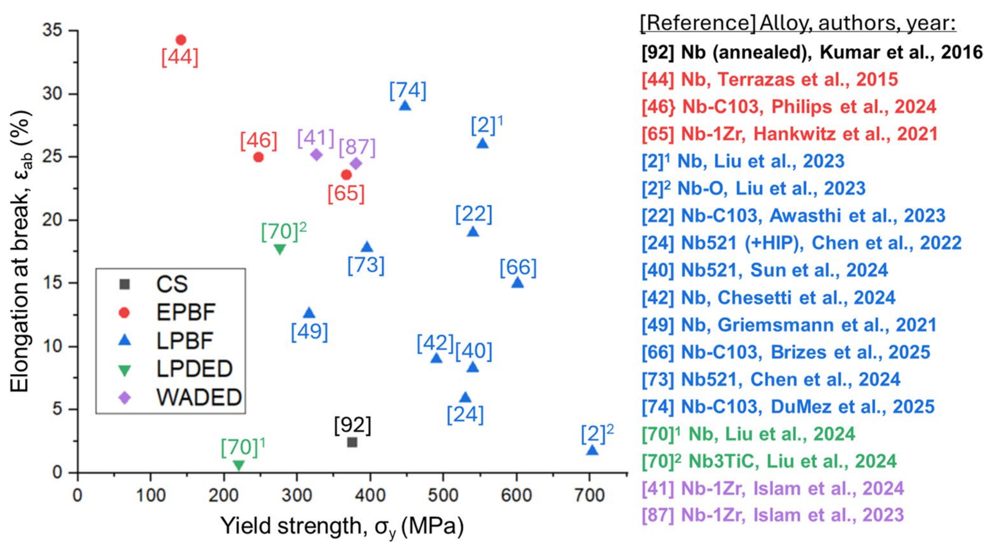

- As shown in Figs. 7 and 17, LPBF resulted in the highest as-built tensile strengths, whereas those made by EPBF and WADED consistently exhibited high ductility.
- The primary strengthening mechanisms identified among AM techniques were relative density, grain size, and dislocation density.
- O embrittlement during all AM process was identified as a key contributor to increased strength at the expense of ductility, as was especially apparent in LPDED, and O uptake was most effectively controlled in EPBF and WADED.
- In general, post-processing heat treatments were a method to restore ductility at the expense of strength, but the relative benefits were dependent on the composition, O content, and AM method.

5.2 Challenges and future opportunities

Important challenges and their associated future opportunities are:

- *Limited compositions have been reported for AM Nb alloys*. Only a small subset of Nb-based alloys (> 50 at% Nb) have been explored with AM. Future research should explore a broader range of alloys used in aerospace, nuclear applications, and superconductors. Further, the literature would greatly benefit from having multiple studies investigate each alloy and AM process, reporting in detail the types of defect structures encountered in each AM process. This will help to mitigate outliers and generate a more statistically reliable dataset of process-structure-property relationships.
- *Nb Alloys have intrinsic manufacturing challenges*. Nb alloys have expensive raw materials that AM can better utilize compared to subtractive machining. Nb's high melting point also confers excellent thermal stability. However, it demands a high energy input in fusion-based AM, which can result in changes to composition, unstable melt pool dynamics, and increased porosity in LPBF and laser DED. Despite Nb's high ductility, the rapid cooling from melt inherent to AM can also cause thermal cracking, especially in samples with high O content. Therefore, future efforts should utilize the unique advantages of EPBF at high ambient temperatures as well as solid-state AM processes like CS.
- *Nb suffers from oxidation and interstitial embrittlement*. Nb has a strong affinity for interstitials including O, N, C, and H. All AM approaches must carefully control O exposure, as even trace levels can lead to embrittlement that severely degrades ductility and toughness. O uptake can be reduced through alloyant addition (e.g. Si, Cr, Hf, and Ti) and alloyant selection can be aided through ML-assisted FP calculations. Further, process modifications are required, such as mitigating O atmospheres during LPBF, LPDED, and CS, as well as utilizing post-processing treatments that reduce pathways for O ingress, such as HIP and environmental barrier coatings.
- *Computational modeling for Nb alloy AM process optimization is understudied*. Optimizing AM processes for Nb alloys remains challenging due to sparse reported experimental and computational data on the interplay between Nb alloy composition, process parameters, and build geometry. More computational studies are needed that model Nb alloys across the scales of FP, PF, and FEM modeling. Trial-and-error AM process parameter selection can be improved if combined with multi-scale models and physics-informed ML to predict melt pool dynamics, solidification behavior, defect formation, and residual stresses. To reliably translate model predictions into AM, validation using process monitoring, characterization, and iterative feedback loops are essential. Without such a validation infrastructure, the integration of ML-driven into industrial-scale AM of Nb alloys will remain limited.

Acknowledgements The authors are grateful for support from the Roux Institute, the Alfond Foundation at Northeastern University, and Northeastern University's Tier 1 program.

Author contributions T.K. and C.Z. wrote the main manuscript text with supplementary contributions from A.N. All authors co-designed the scope of research and reviewed the manuscript.

Funding Open access funding provided by Northeastern University Library

Data availability Data will be made available on request.

Declarations

Conflict of interest The authors declare no competing interests.

References

1. Snead LL, Hoelzer DT, Rieth M, Nemith AA (2019) Structural alloys for nuclear energy applications. Elsevier, pp 585–640. https://doi.org/10.1016/B978-0-12-397046-6.00013-7
2. Liu M, Zhang J, Chen C, Geng Z, Wu Y, Li D, Zhang T, Guo Y (2023) Additive manufacturing of pure niobium by laser powder bed fusion: microstructure, mechanical behavior and oxygen assisted embrittlement. Mater Sci Engineering: A 866. https://doi.org/10.1016/j.msea.2023.144691
3. Yan D, Song K, Sun H, Wu S, Zhao K, Zhang H, Yuan S, Kim JT, Chawake N, Renk O (2020) Microstructures, mechanical properties, and corrosion behaviors of refractory high-entropy ReTaWNbMo alloys. J Mater Eng Perform 29:399–409. https://doi.org/10.1007/s11665-019-04540-y
4. Xiong W, Guo AX, Zhan S, Liu C-T, Cao SC (2023) Refractory high-entropy alloys: a focused review of preparation methods and properties. J Mater Sci Technol 142:196–215. https://doi.org/10.1016/j.jmst.2022.08.046

5. Gou S, Gao M, Shi Y, Li S, Fang Y, Chen X, Chen H, Yin W, Liu J, Lei Z (2023) Additive manufacturing of ductile refractory high-entropy alloys via phase engineering. Acta Mater 248:118781. https://doi.org/10.1016/j.actamat.2023.118781
6. Wang F, Yuan T, Li R, Lin S, Xie Z, Li L, Cristino V, Xu R, Liu B (2023) Comparative study on microstructures and mechanical properties of ultra ductility single-phase Nb40Ti40Ta20 refractory medium entropy alloy by selective laser melting and vacuum arc melting. J Alloys Compd 942:169065. https://doi.org/10.1016/j.jallcom.2023.169065
7. Singh P, Vela B, Ouyang G, Argibay N, Cui J, Arroyave R, Johnson DD (2023) A ductility metric for refractory-based multi-principal-element alloys. Acta Mater 257:119104. https://doi.org/10.1016/j.actamat.2023.119104
8. Joshi K, Kumar P (2024) Strength behavior of niobium-based refractory systems. Jom 76:6277–6301. https://doi.org/10.1007/s11837-024-06847-1
9. Ma C, Gui Y, Wang Y, Dong X, Huang Y, Fu H, Shu G (2024) Processing, defect formation, microstructure, and mechanical properties of additively manufactured refractory metals: a review. J Mater Eng Perform. https://doi.org/10.1007/s11665-024-10566-8
10. Philips NR, Carl M, Cunningham NJ (2020) New opportunities in refractory alloys. Metall Mater Trans A 51:3299–3310. https://doi.org/10.1007/s11661-020-05803-3
11. Abdullah MR, Peng Z (2024) Review and perspective on additive manufacturing of refractory high entropy alloys. Mater Today Adv 22:100497. https://doi.org/10.1016/j.mtadv.2024.100497
12. Shabalin IL (2022) Ultra-high temperature materials IV. 1 ed., Springer Cham. https://doi.org/10.1007/978-3-031-07175-1
13. Yang P-J, Li Q-J, Tsuru T, Ogata S, Zhang J-W, Sheng H-W, Shan Z-W, Sha G, Han W-Z, Li J, Ma E (2019) Mechanism of hardening and damage initiation in oxygen embrittlement of body-centred-cubic niobium. Acta Mater 168:331–342. https://doi.org/10.1016/j.actamat.2019.02.030
14. Nico C, Monteiro T, Graça MPF (2016) Niobium oxides and niobates physical properties: review and prospects. Prog Mater Sci 80:1–37. https://doi.org/10.1016/j.pmatsci.2016.02.001
15. Banno N (2023) Low-temperature superconductors: Nb3Sn, Nb3Al, and NbTi. Superconductivity 6. https://doi.org/10.1016/j.supcon.2023.100047
16. Momma K, Izumi F (2011) VESTA 3 for three-dimensional visualization of crystal, volumetric and morphology data. J Appl Crystallogr 44:1272–1276. https://doi.org/10.1107/S0021889811038970
17. von Rennenberg T, Yu Y, Fraccascia L, Yazan DM (2024) Circularity reinforcement of critical raw materials in Europe: a case of niobium. Circular Econ Sustain 1–24. https://doi.org/10.1007/s43615-024-00369-3
18. Mackay D, Simandl G (2015) Niobium and tantalum: Geology, markets, and supply chains. Symposium on critical and strategic materials 13–22. https://cmscontent.nrs.gov.bc.ca/geoscience/publicationcatalogue/Paper/BCGS_P2015-03-03_Mackay.pdf
19. Gómez M, Li J, Zeng X, (2024) Niobium: the unseen element-A comprehensive examination of its evolution, global dynamics, and outlook. Resources Conserv Recycl 209:107744. https://doi.org/10.1016/j.resconrec.2024.107744
20. McCaffrey DM, Nassar NT, Jowitt SM, Padilla AJ, Bird LR (2023) Embedded critical material flow: the case of niobium, the United States, and China. Res, Conserv Recycl 188:106698. https://doi.org/10.1016/j.resconrec.2022.106698
21. Mireles O (2021) Additive manufacture of refractory metals for aerospace applications. AIAA Propuls Energy 2021 Forum 3234. https://ntrs.nasa.gov/citations/20210018657
22. Awasthi PD, Agrawal P, Haridas RS, Mishra RS, Stawovy MT, Ohm S, Imandoust A (2022) Mechanical properties and microstructural characteristics of additively manufactured C103 niobium alloy. Mater Sci Engineering: A 831. https://doi.org/10.1016/j.msea.2021.142183
23. Funch CV, Proust G (2024) Laser-based additive manufacturing of refractory metals and their alloys: a review. Additive Manuf 94. https://doi.org/10.1016/j.addma.2024.104464
24. Chen J, Ding W, Tao Q, Ma C, Zhang C, Chen G, Qin M, Qu X (2022) Laser powder bed fusion of a Nb-based refractory alloy: Microstructure and tensile properties. Mater Sci Engineering: A 843. https://doi.org/10.1016/j.msea.2022.143153
25. Senkov O, Rao S, Butler T, Chaput K (2019) Ductile Nb alloys with reduced density and cost. J Alloys Compd 808:151685. https://doi.org/10.1016/j.jallcom.2019.151685
26. Liu W, Huang S, Ye C, Jia L, Kang Y, Sha J, Chen B, Wu Y, Xiong H (2023) Progress in Nb-Si ultra-high temperature structural materials: a review. J Mater Sci Technol 149:127–153. https://doi.org/10.1016/j.jmst.2022.11.022
27. Li Y, Lin X, Hu Y, Gao X, Yu J, Dong H (2024) Alloying on the high-temperature oxidation behavior of Nb-Ti-Si-based alloy additively manufactured by laser directed energy deposition. Int J Refract Met Hard Mater 121:106682. https://doi.org/10.1016/j.ijrmhm.2024.106682
28. Ma R, Guo X (2021) Influence of molybdenum contents on the microstructure, mechanical properties and oxidation behavior of multi-elemental Nb–Si based ultrahigh temperature alloys. Intermetallics 129:107053. https://doi.org/10.1016/j.intermet.2020.107053
29. Williams JC, Boyer RR (2020) Opportunities and issues in the application of titanium alloys for aerospace components. Metals 10:705. https://doi.org/10.3390/met10060705
30. Jiang G, Xu D, Yang W, Liu L, Zhi Y, Yang J (2022) High-temperature corrosion of Zr–Nb alloy for nuclear structural materials. Prog Nucl Energy 154:104490. https://doi.org/10.1016/j.pnucene.2022.104490
31. Sun C, Wang Y, McMurtrey MD, Jerred ND, Liou F, Li J (2021) Additive manufacturing for energy: a review. Appl Energy 282:116041. https://doi.org/10.1016/j.apenergy.2020.116041
32. Fischer M, Laheurte P, Acquier P, Joguet D, Peltier L, Petithory T, Anselme K, Mille P (2017) Synthesis and characterization of Ti-27.5 Nb alloy made by CLAD® additive manufacturing process for biomedical applications. Mater Sci Engineering: C 75:341–348. https://doi.org/10.1016/j.msec.2017.02.060
33. da Silva LRR, Sales WF, Campos FAR, de Sousa JAG, Davis R, Singh A, Coelho RT, Borgohain B (2021) A comprehensive review on additive manufacturing of medical devices. Progress Additive Manuf 6:517–553. https://doi.org/10.1007/s40964-021-00188-0
34. Donoso J, Reed-Hill R (1976) Slow strain-rate embrittlement of niobium by Oxygen. Metall Trans A 7:961–965. https://doi.org/10.1007/BF02644061
35. Kumaravel M, Eynolghozzat Y, Gussone J, Yan F, Lordejani AA, Haubrich J, Requena G, Berglund IS, Guagliano M, Bagherifard S (2024) Elucidating the challenges in the development and deployment of refractory complex concentrated alloys for additive manufacturing. Additive Manuf 89:104286. https://doi.org/10.1016/j.addma.2024.104286
36. Gradl P, Protz C (2019) Channel wall nozzle manufacturing technology advancements for liquid rocket engines. 70th International Astronautical Congress M19-7683. https://ntrs.nasa.gov/api/citations/20190033314/downloads/20190033314.pdf
37. Gradl P, Tinker DC, Park A, Mireles OR, Garcia M, Wilkerson R, McKinney C (2022) Robust metal additive manufacturing process selection and development for aerospace components. J Mater Eng Perform 31:6013–6044. https://doi.org/10.1007/s11665-022-06850-0
38. Mukherjee P, Gabourel A, Firdosy SA, Hofmann DC, Moridi A (2024) Additive manufacturing of refractory metals and carbides

for extreme environments: an overview. Sci Technol Weld Joining 29:99–115. https://doi.org/10.1177/13621718241235471
39. DebRoy T, Wei HL, Zuback JS, Mukherjee T, Elmer JW, Milewski JO, Beese AM, Wilson-Heid A, De A, Zhang W (2018) Additive manufacturing of metallic components – Process, structure and properties. Prog Mater Sci 92:112–224. https://doi.org/10.1016/j.pmatsci.2017.10.001
40. Sun Y, Liu J, Wang J, Zhang K, Chen L, Hao M (2024) A Nb521 alloy processed by selective laser melting: microstructure and tensile properties. Vacuum 219. https://doi.org/10.1016/j.vacuum.2023.112726
41. Islam S, Jadhav S, Park T, Pourboghrat F, Fan X, Liaw PK, Kim DB (2024) Crystal plasticity approach for predicting mechanical responses in wire-arc directed energy deposition of NbZr1 refractory alloy. Additive Manuf 84:104107. https://doi.org/10.1016/j.addma.2024.104107
42. Chesetti A, Banerjee S, Krishna KVM, Soni V, Varahabhatla SM, Sharma A, Mantri SA, Nartu MSKKY, Dahotre NB, Banerjee R (2024) Assessing the factors underlying the high yield strength of laser powder bed fusion processed niobium. Mater Sci Engineering: A 910. https://doi.org/10.1016/j.msea.2024.146896
43. Yao L, Wang L, Song X, Cui R, Li B, Lv Q, Luo L, Su Y, Guo J, Fu H (2022) Microstructure evolution and toughening mechanism of a Nb-18Si-5HfC eutectic alloy created by selective laser melting. Mater (Basel) 15. https://doi.org/10.3390/ma15031190
44. Terrazas CA, Mireles J, Gaytan SM, Morton PA, Hinojos A, Frigola P, Wicker RB (2015) Fabrication and characterization of high-purity niobium using electron beam melting additive manufacturing technology. Int J Adv Manuf Technol. https://doi.org/10.1007/s00170-015-7767-x
45. Yang J, Huang Y, Liu B, Guo C, Sun J (2021) Precipitation behavior in a Nb-5 W-2Mo-1Zr niobium alloy fabricated by electron beam selective melting. Mater Charact 174. https://doi.org/10.1016/j.matchar.2021.111019
46. Philips N, Rock C, Cunningham N, Cooper J, Horn T (2024) Electron beam powder bed fusion of ATI C103TM refractory alloy. Metall Mater Trans A 55:2472–2484. https://doi.org/10.1007/s11661-024-07411-x
47. Colón BJ, Watanabe KI, Hobbs TJ, Romnes CJ, Mireles OR, Murr LE, Medina F (2024) Parameter development and characterization of laser powder directed energy deposition of Nb – Alloy C103 for thin wall geometries. J Mater Res Technol 30:5028–5039. https://doi.org/10.1016/j.jmrt.2024.04.200
48. Liao J, Wei Z, Yu F, Yu Y, Peng H, Sha J (2023) Microstructure and fracture behaviours of Nb–16Si ultra-high temperature alloy fabricated by laser directed energy deposition. Intermetallics 157. https://doi.org/10.1016/j.intermet.2023.107874
49. Griemsmann T, Abel A, Hoff C, Hermsdorf J, Weinmann M, Kaierle S (2021) Laser-based powder bed fusion of niobium with different build-up rates. Int J Adv Manuf Technol 114:305–317. https://doi.org/10.1007/s00170-021-06645-y
50. Creative Commons (2026) Attribution 4.0 International. https://creativecommons.org/licenses/by/4.0/
51. Merchant A, Batzner S, Schoenholz SS, Aykol M, Cheon G, Cubuk ED (2023) Scaling deep learning for materials discovery. Nature 624:80–85. https://doi.org/10.1038/s41586-023-06735-9
52. Li J, Lim K, Yang H, Ren Z, Raghavan S, Chen P-Y, Buonassisi T, Wang X (2020) AI applications through the whole life cycle of material discovery. Matter 3:393–432. https://doi.org/10.1016/j.matt.2020.06.011
53. Jain A, Ong SP, Hautier G, Chen W, Richards WD, Dacek S, Cholia S, Gunter D, Skinner D, Ceder G (2013) Commentary: the materials project: a materials genome approach to accelerating materials innovation. APL Mater 1. https://doi.org/10.1063/1.4812323
54. Gunasegaram DR, Murphy A, Barnard A, DebRoy T, Matthews M, Ladani L, Gu D (2021) Towards developing multiscale-multiphysics models and their surrogates for digital twins of metal additive manufacturing. Additive Manuf 46:102089. https://doi.org/10.1016/j.addma.2021.102089
55. Yan W, Lin S, Kafka OL, Lian Y, Yu C, Liu Z, Yan J, Wolff S, Wu H, Ndip-Agbor E (2018) Data-driven multi-scale multi-physics models to derive process–structure–property relationships for additive manufacturing. Comput Mech 61:521–541. https://doi.org/10.1007/s00466-018-1539-z
56. Hashemi SM, Parvizi S, Baghbanijavid H, Tan AT, Nematollahi M, Ramazani A, Fang NX, Elahinia M (2022) Computational modelling of process–structure–property–performance relationships in metal additive manufacturing: a review. Int Mater Rev 67:1–46. https://doi.org/10.1080/09506608.2020.1868889
57. Wang C, Tan XP, Tor SB, Lim C (2020) Machine learning in additive manufacturing: State-of-the-art and perspectives. Additive Manuf 36:101538. https://doi.org/10.1016/j.addma.2020.101538
58. Meng L, McWilliams B, Jarosinski W, Park H-Y, Jung Y-G, Lee J, Zhang J (2020) Machine learning in additive manufacturing: a review. Jom 72:2363–2377. https://doi.org/10.1007/s11837-020-04155-y
59. Phua A, Davies C, Delaney GW (2022) A digital twin hierarchy for metal additive manufacturing. Comput Ind 140:103667. https://doi.org/10.1016/j.compind.2022.103667
60. Liu B, Zhang P, Yan H, Lu Q, Shi H, Liu Z, Wu D, Sun T, Li R, Wang Q (2024) A review on manufacturing pure refractory metals by selective laser melting. J Mater Eng Perform 33:9945–9975. https://doi.org/10.1007/s11665-024-09693-z
61. Talignani A, Seede R, Whitt A, Zheng S, Ye J, Karaman I, Kirka MM, Katoh Y, Wang YM (2022) A review on additive manufacturing of refractory tungsten and tungsten alloys. Additive Manuf 58:103009. https://doi.org/10.1016/j.addma.2022.103009
62. Cheng W, Ji L, Zhang L, Wang H, Sun W (2023) Refractory high-entropy alloys fabricated using laser technologies: a concrete review. J Mater Res Technol 24:7497–7524. https://doi.org/10.1016/j.jmrt.2023.05.037
63. Schoinochoritis B, Chantzis D, Salonitis K (2017) Simulation of metallic powder bed additive manufacturing processes with the finite element method: a critical review. Proc Institution Mech Eng Part B: J Eng Manuf 231:96–117. https://doi.org/10.1177/0954405414567522
64. Ladani L, Sadeghilaridjani M (2021) Review of powder bed fusion additive manufacturing for metals. Metals 11. https://doi.org/10.3390/met11091391
65. Hankwitz JP, Ledford C, Rock C, O'Dell S, Horn TJ (2021) Electron beam melting of niobium alloys from blended powders. Mater (Basel) 14. https://doi.org/10.3390/ma14195536
66. Brizes E, Milner J, Young-Dohe E, Garg A, Noebe R (2025) Effect of Temperature on Tensile properties of laser powder bed fusion additively manufactured niobium alloy C103. Metall Mater Trans A 56:928–941. https://doi.org/10.1007/s11661-024-07683-3
67. Scipioni Bertoli U, Wolfer AJ, Matthews MJ, Delplanque J-PR, Schoenung JM (2017) On the limitations of volumetric energy density as a design parameter for selective laser melting. Mater Design 113:331–340. https://doi.org/10.1016/j.matdes.2016.10.037
68. Reith M, Franke M, Körner C (2023) Impact of the acceleration voltage on the processing of γ-TiAl via electron beam powder bed fusion. Progress Additive Manuf 9:1425–1436. https://doi.org/10.1007/s40964-023-00499-4
69. Dinita A, Neacsa A, Portoaca AI, Tanase M, Ilinca CN, Ramadan IN (2023) Additive manufacturing post-processing treatments, a review with emphasis on mechanical characteristics. Mater (Basel) 16. https://doi.org/10.3390/ma16134610

70. Liu D, Liu W, Wang Y, Yu Y, Sha J (2024) Grain refinement and strengthening of additively manufactured Nb by doping TiC nanoparticle prepared via laser directed energy deposition. Additive Manuf 84. https://doi.org/10.1016/j.addma.2024.104129
71. Candela S, Rebesan P, De Bortoli D, Carmignato S, Zanini F, Candela V, Dima R, Pepato A, Weinmann M, Bettini P (2024) Pure niobium manufactured by laser-based powder bed fusion: influence of process parameters and supports on as-built surface quality. Int J Adv Manuf Technol 131:4469–4482. https://doi.org/10.1007/s00170-024-13249-9
72. Cardozo EP, D'Oliveira ASCM, Attallah MM (2024) Laser powder bed fusion of pure Nb and Nb + WC powder mixture. Int J Refract Met Hard Mater 122. https://doi.org/10.1016/j.ijrmhm.2024.106687
73. Chen J, Liu C, Wang Y, Ding W, Tao Q, Chen G, Cai W, Qin M, Qu X (2024) Strong and ductile niobium-based refractory alloy via deformable zirconia nanoparticles. Int J Refract Met Hard Mater 118. https://doi.org/10.1016/j.ijrmhm.2023.106451
74. DuMez T, Stawovy MT, Ohm S (2025) Tensile properties of R512E coated Nb C103 manufactured using laser powder bed fusion (L-PBF). Int J Refract Met Hard Mater 128. https://doi.org/10.1016/j.ijrmhm.2024.106959
75. Guo Y, Jia L, Sun S, Kong B, Liu J, Zhang H (2016) Rapid fabrication of Nb-Si based alloy by selective laser melting: microstructure, hardness and initial oxidation behavior. Mater Design 109:37–46. https://doi.org/10.1016/j.matdes.2016.07.048
76. Martinez E, Murr LE, Hernandez J, Pan X, Amato K, Frigola P, Terrazas C, Gaytan S, Rodriguez E, Medina F, Wicker RB (2013) Microstructures of niobium components fabricated by electron beam melting. Metallogr Microstruct Anal 2:183–189. https://doi.org/10.1007/s13632-013-0073-9
77. Gao R, Peng H, Guo H, Chen B (2024) Insights into Nb-silicide-based in-situ composite processed by electron beam powder bed fusion. J Mater Process Technol 330. https://doi.org/10.1016/j.jmatprotec.2024.118488
78. Wennersten K, Xu J, Armakavicius N, Wiberg A, Nadali Najafabadi H, Moverare J (2024) Feasibility of melting NbC using electron beam powder bed fusion. Adv Eng Mater 26. https://doi.org/10.1002/adem.202301388
79. Bowling LS, Philips NR, Matejczyk DE, Skelton JM, Fitz-Gerald JM, Agnew SR (2024) A unified model of tensile and creep deformation for use in niobium alloy materials selection and design for high-temperature applications. Materialia 38. https://doi.org/10.1016/j.mtla.2024.102210
80. Bowling LS, Wang AT, Philips NR, Riffe WT, Matejczyk DE, Skelton JM, Hopkins PE, Fitz-Gerald JM, Agnew SR (2024) Thermophysical modeling of niobium alloys informs materials selection and design for high-temperature applications. Mater Design 248. https://doi.org/10.1016/j.matdes.2024.113456
81. Piscopo G, Iuliano L (2022) Current research and industrial application of laser powder directed energy deposition. Int J Adv Manuf Technol 119:6893–6917. https://doi.org/10.1007/s00170-021-08596-w
82. Hamrani A, Bouarab FZ, Agarwal A, Ju K, Akbarzadeh H (2023) Advancements and applications of multiple wire processes in additive manufacturing: a comprehensive systematic review. Virtual Phys Prototyp 18. https://doi.org/10.1080/17452759.2023.2273303
83. Tomar B, Shiva S, Nath T (2022) A review on wire arc additive manufacturing: Processing parameters, defects, quality improvement and recent advances. Mater Today Commun 31. https://doi.org/10.1016/j.mtcomm.2022.103739
84. Zahidin MR, Yusof F, Abdul Rashid SH, Mansor S, Raja S, Jamaludin MF, Manurung YHP, Adenan MS, Syahriah Hussein NI (2023) Research challenges, quality control and monitoring strategy for wire arc additive manufacturing. J Mater Res Technol 24:2769–2794. https://doi.org/10.1016/j.jmrt.2023.03.200
85. Islam S, Ahsan MRU, Seo G-J, Lee H-J, Park T, Pourboghrat F, Kim DB (2023) Investigations of microstructure and mechanical properties in wire + arc additively manufactured niobium–zirconium alloy. Adv Eng Mater 25. https://doi.org/10.1002/adem.202201633
86. Zhou YH, Lin SF, Hou YH, Wang DW, Zhou P, Han PL, Li YL, Yan M (2018) Layered surface structure of gas-atomized high Nb-containing TiAl powder and its impact on laser energy absorption for selective laser melting. Appl Surf Sci 441:210–217. https://doi.org/10.1016/j.apsusc.2018.01.296
87. Prabhune B, Panicker N, Jordan B, Lim B, Snyder K, Delchini M, See ND, Nag S, Plotnikov Y, Lee Y (2025) Multi-physics melt pool modeling and process optimization for laser direct energy deposition of Nb-based refractory C103: Defect formation, geometric precision, and process mapping. J Manuf Process 154:444–461. https://doi.org/10.1016/j.jmapro.2025.09.082
88. Liu W, Sha J (2016) Failure mode transition of Nb phase from cleavage to dimple/tear in Nb-16Si-based alloys prepared via spark plasma sintering. Mater Design 111:301–311. https://doi.org/10.1016/j.matdes.2016.08.087
89. Amiri M, Soto Leytan KN, Apelian D, Mumm DR, Valdevit L (2024) Controlling splat boundary network evolution towards the development of strong and ductile cold sprayed refractory metals: The role of powder characteristics. Mater Sci Engineering: A 902. https://doi.org/10.1016/j.msea.2024.146559
90. Champagne VK Jr, Ozdemir OC, Nardi A (2021) Practical cold spray. Springer. https://doi.org/10.1007/978-3-030-70056-0
91. Nastic A, MacDonald D, Jodoin B (2020) Cold spray in the realm of additive manufacturing. Springer, pp 33–85. https://doi.org/10.1007/978-3-030-42756-6_3
92. Hemeda AA, Zhang C, Hu XY, Fukuda D, Cote D, Nault IM, Nardi A, Champagne VK, Ma Y, Palko JW (2021) Particle-based simulation of cold spray: influence of oxide layer on impact process. Additive Manuf 37. https://doi.org/10.1016/j.addma.2020.101517
93. Kumar S, Jyothirmayi A, Wasekar N, Joshi SV (2016) Influence of annealing on mechanical and electrochemical properties of cold sprayed niobium coatings. Surf Coat Technol 296:124–135. https://doi.org/10.1016/j.surfcoat.2016.04.027
94. Kumar S, Ramakrishna M, Chavan NM, Joshi SV (2017) Correlation of splat state with deposition characteristics of cold sprayed niobium coatings. Acta Mater 130:177–195. https://doi.org/10.1016/j.actamat.2017.03.023
95. Kumar S, Dhavale AS, Chavan NM, Acharya S (2022) Superconducting niobium coating deposited using cold spray. Mater Lett 312. https://doi.org/10.1016/j.matlet.2022.131715
96. Yamanaka M, Shimada K (2023) A novel manufacture of niobium SRF cavities by cold spray. 21th Int Conf RF Supercond. https://doi.org/10.18429/JACoW-SRF2023-TUPTB052
97. Nault IM, Ellingsen M, Nardi A (2024) Prediction of geometry-induced porosity in cold spray additive manufacturing of leading edges. J Therm Spray Technol 33:839–857. https://doi.org/10.1007/s11666-024-01730-6
98. Roper BET (2023) Mechanisms, microstructures, and mechanical behavior in cold spray refractory metals. Dissertation, The University of Alabama. https://www.proquest.com/dissertations-theses/mechanisms-microstructures-mechanical-behavior/docview/2924898408/se-2?accountid=12826
99. Sotiropoulos NH, Nault IM, Blassino AA, Nicholas MB (2024) Shot peening-assisted cold spray-enabling 'helium performance' with nitrogen. J Therm Spray Technol 33:2262–2277. https://doi.org/10.1007/s11666-024-01854-9

100. Broitman E (2016) Indentation hardness measurements at macro-, micro-, and nanoscale: a critical overview. Tribol Lett 65. https://doi.org/10.1007/s11249-016-0805-5
101. Liu L, Ding Q, Zhong Y, Zou J, Wu J, Chiu Y-L, Li J, Zhang Z, Yu Q, Shen Z (2018) Dislocation network in additive manufactured steel breaks strength–ductility trade-off. Mater Today 21:354–361. https://doi.org/10.1016/j.mattod.2017.11.004
102. Keller T, Campbell Q, Hayrikyan D, Murphy K, Fitchorova O, Lesko J, Post N, Neils A (2025) Strength, microhardness, and microstructure analysis of 316L stainless steel manufactured via hybrid laser wire and laser powder bed additive. J Manuf Process 150:1–9. https://doi.org/10.1016/j.jmapro.2025.06.037
103. Li Z, Cui Y, Yan W, Zhang D, Fang Y, Chen Y, Yu Q, Wang G, Ouyang H, Fan C, Guo Q, Xiong D-B, Jin S, Sha G, Ghoniem N, Zhang Z, Wang YM (2021) Enhanced strengthening and hardening via self-stabilized dislocation network in additively manufactured metals. Mater Today 50:79–88. https://doi.org/10.1016/j.mattod.2021.06.002
104. Ashby MF (1970) The deformation of plastically non-homogeneous materials. Philosophical Magazine: J Theor Exp Appl Phys 21:399–424. https://doi.org/10.1080/14786437008238426
105. Kuhlmann-Wilsdorf D (1999) The theory of dislocation-based crystal plasticity. Philos Mag A 79:955–1008. https://doi.org/10.1080/01418619908210342
106. Guo H, Guo X (2011) Microstructure evolution and room temperature fracture toughness of an integrally directionally solidified Nb–Ti–Si based ultrahigh temperature alloy. Scripta Mater 64:637–640. https://doi.org/10.1016/j.scriptamat.2010.12.008
107. Saleh JM, Matlub MH (1974) Oxidation of titanium, tantalum, and niobium films by oxygen and nitrous oxide. J Phys Chem 78:2486–2489
108. Nourian A, Beamer C, Muftu S (2024) Effects of post-deposition processing on static and cyclic performance of cold sprayed 6061 aluminum alloy. Additive Manuf 88. https://doi.org/10.1016/j.addma.2024.104246
109. Boese SM Laser Assisted Cold Spray of Aluminum Alloy 6061. Dissertation, Northeastern, University (2024) https://www.proquest.com/dissertations-theses/laser-assisted-cold-spray-aluminum-alloy-6061/docview/3098002079/se-2?accountid=12826
110. Zhang Y, Fu T, Yu L, Cui K, Wang J, Shen F, Zhang X, Zhou K (2022) Anti-corrosion coatings for protecting Nb-based alloys exposed to oxidation environments: a review. Met Mater Int 29:1–17. https://doi.org/10.1007/s12540-022-01222-8
111. Oliveira RM, Hoshida L, Oliveira AC, Silva MMNF, Pichon L, Santos NM (2017) Evaluation of the resistance to oxidation of niobium treated by high temperature nitrogen plasma based ion implantation. Surf Coat Technol 312:110–116. https://doi.org/10.1016/j.surfcoat.2016.10.012
112. Shen F, Zhang Y, Yu L, Fu T, Wang J, Wang H, Cui K (2021) Microstructure and oxidation behavior of Nb-Si-based alloys for ultrahigh temperature applications: a comprehensive review. Coatings 11. https://doi.org/10.3390/coatings11111373
113. Ramachandran K, Jayakody YC, Jayaseelan DD (2023) Oxidation behaviour and its effect on fracture toughness of Niobium metal. Int J Refract Met Hard Mater 110. https://doi.org/10.1016/j.ijrmhm.2022.106033
114. Borowski T, Zielińska K, Spychalski M, Adamczyk-Cieślak B, Żrodowski Ł (2023) Effect of oxidation temperature on the properties of niobium in view of its biomedical applications. Surf Coat Technol 473. https://doi.org/10.1016/j.surfcoat.2023.129911
115. Lei S, Liu J, Liu D, Zhang K, Yang R, Yan Z, Zhang X, Li W (2023) Diffusion barrier effect of Ta or TaSi2 layer at the MoSi2/Nb-based alloy interface. Corros Sci 216. https://doi.org/10.1016/j.corsci.2023.111090
116. Holgate CS, Frey C, Endsley MA, Suzuki A, Levi CG, Pollock TM (2025) Design of an alumina forming coating for Nb-base refractory alloys. Mater Design 251. https://doi.org/10.1016/j.matdes.2025.113652
117. Xie H, Champagne VK, Zhong W, Clifford B, Liu S, Hu L, Zhao JC, Clarke DR (2023) Design, fabrication, and screening of environmental-thermal barrier coatings prepared by ultrafast high-temperature sintering. Adv Funct Mater 34. https://doi.org/10.1002/adfm.202309978
118. Shu J, Dong Z, Zheng C, Sun A, Yang S, Han T, Liu Y, Wang Z, Wang S, Liu Y (2022) High-throughput experiment-assisted study of the alloying effects on oxidation of Nb-based alloys. Corros Sci 204. https://doi.org/10.1016/j.corsci.2022.110383
119. Liang Z, Jiang M, Gong J, Olson GB (2024)(2024 of Conference) Innovative design of advanced niobium-based alloys for extreme high-temperature applications. In: Advances in Materials, Manufacturing, and Repair for Power Plants: Proceedings from the Tenth International Conference 592–599. https://doi.org/10.31399/asm.cp.am-epri-2024p0592
120. Peters AB, Zhang D, Chen S, Ott C, Oses C, Curtarolo S, McCue I, Pollock TM, Eswarappa Prameela S (2024) Materials design for hypersonics. Nat Commun 15:3328. https://doi.org/10.1038/s41467-024-46753-3
121. Bukhanovsky V, Mamuzić I (2003) The effect of temperature on mechanical characteristics of niobium alloys of the system Nb-W-Mo-Zr. Metalurgija 42:85–90. https://hrcak.srce.hr/file/189694
122. Reynolds C, Pollock TM, Van der Ven A (2024) Solute-solute interactions in dilute Nb-XO alloys from first principles. Acta Mater 266:119621. https://doi.org/10.1016/j.actamat.2023.119621
123. Jain V, Das K, Chaudhuri A, Manna M, Pal S, Ghosh M (2023) Modelling of thermal behaviour in niobium during electron beam welding. Mater Today Commun 37. https://doi.org/10.1016/j.mtcomm.2023.107020
124. Singh D, Sharma P, Jindal S, Kumar P, Kumar P, Parashar A (2019) Atomistic simulations to study crack tip behaviour in single crystal of bcc niobium and hcp zirconium. Curr Appl Phys 19:37–43. https://doi.org/10.1016/j.cap.2018.11.002
125. Parashar A, Singh D (2017) Molecular dynamics based study of an irradiated single crystal of niobium. Comput Mater Sci 131:48–54. https://doi.org/10.1016/j.commatsci.2017.01.028
126. Singh D, Sharma P, Parashar A (2020) Atomistic simulations to study point defect dynamics in bi-crystalline niobium. Mater Chem Phys 255. https://doi.org/10.1016/j.matchemphys.2020.123628
127. Derlet PM, Nguyen-Manh D, Dudarev S (2007) Multiscale modeling of crowdion and vacancy defects in body-centered-cubic transition metals. Phys Rev B—Condensed Matter Mater Phys 76:054107. https://doi.org/10.1103/PhysRevB.76.054107
128. Yang C, Qi L (2019) Modified embedded-atom method potential of niobium for studies on mechanical properties. Comput Mater Sci 161:351–363. https://doi.org/10.1016/j.commatsci.2019.01.047
129. Senkov O, Rao S, Butler T, Daboiku T, Chaput K (2020) Effect of Fe additions on the microstructure and properties of Nb-Mo-Ti alloys. Int J Refract Met Hard Mater 89:105221. https://doi.org/10.1016/j.ijrmhm.2020.105221
130. Moelans N, Blanpain B, Wollants P (2008) An introduction to phase-field modeling of microstructure evolution. Calphad 32:268–294. https://doi.org/10.1016/j.calphad.2007.11.003
131. Zhao Y (2023) Understanding and design of metallic alloys guided by phase-field simulations. npj Comput Mater 9:94. https://doi.org/10.1038/s41524-023-01038-z
132. Fallah V, Amoorezaei M, Provatas N, Corbin SF, Khajepour A (2012) Phase-field simulation of solidification morphology in laser powder deposition of Ti–Nb alloys. Acta Mater 60:1633–1646. https://doi.org/10.1016/j.actamat.2011.12.009
133. Cheng Y, Wang G, Qiu Z, Zheng Z, Zeng D, Tang X, Shi R, Uddagiri M, Steinbach I (2024) Multi-physics simulation of non-equilibrium solidification in Ti-Nb alloy during selective laser melting. Acta Mater 272. https://doi.org/10.1016/j.actamat.2024.119923

134. Zhang Z, Yao XX, Ge P (2020) Phase-field-model-based analysis of the effects of powder particle on porosities and densities in selective laser sintering additive manufacturing. Int J Mech Sci 166:105230. https://doi.org/10.1016/j.ijmecsci.2019.105230
135. Luo Z, Zhao Y (2018) A survey of finite element analysis of temperature and thermal stress fields in powder bed fusion additive manufacturing. Additive Manuf 21:318–332. https://doi.org/10.1016/j.addma.2018.03.022
136. Zhang X, Ye W, Mushongera L, Liao Y (2022) Unravelling heterogeneities in sub-grain cellular structure and micromechanical response of additive manufactured Ti-Nb alloys. Additive Manuf 59. https://doi.org/10.1016/j.addma.2022.103146
137. Ghosh S, Ma L, Ofori-Opoku N, Guyer JE (2017) On the primary spacing and microsegregation of cellular dendrites in laser deposited Ni-Nb alloys. Model Simul Mat Sci Eng 25. https://doi.org/10.1088/1361-651x/aa7369. https://www.ncbi.nlm.nih.gov/pubmed/39444581
138. Yan W, Lin S, Kafka OL, Yu C, Liu Z, Lian Y, Wolff S, Cao J, Wagner GJ, Liu WK (2018) Modeling process-structure-property relationships for additive manufacturing. Front Mech Eng 13:482–492. https://doi.org/10.1007/s11465-018-0505-y
139. Mohanty T, Chandran KSR, Sparks TD (2023) Machine learning guided optimal composition selection of niobium alloys for high temperature applications. APL Mach Learn 1. https://doi.org/10.1063/5.0129528
140. Xiong Z, Song Z, Li J, Wang H, Zhang X, Liang B, Wang D (2025) Machine learning-driven design of rare metal doped niobium alloys with enhanced strength and ductility. J Mater Res Technol 36:3154–3165. https://doi.org/10.1016/j.jmrt.2025.04.037
141. Wei D, Pang X, Wang J, Li Z, Zong H, Ding X, Lookman T, Sun J (2026) Data-driven design of Nb-W refractory alloys using Transformer-based stress-strain modeling. Acta Mater 309. https://doi.org/10.1016/j.actamat.2026.122123
142. Dong Z, Yu X, Huang Q, Dai L, Mou Z, Zhou C, Zhou H, He Y, Zheng W, Jin L (2026) Machine learning-guided optimization of oxidation resistance in NbTiZr-containing refractory high-entropy alloys. Corros Sci 260. https://doi.org/10.1016/j.corsci.2025.113557
143. Zeng C, Neils A, Lesko J, Post N (2024) Machine learning accelerated discovery of corrosion-resistant high-entropy alloys. Comput Mater Sci 237. https://doi.org/10.1016/j.commatsci.2024.112925
144. Scime L, Beuth J (2018) Anomaly detection and classification in a laser powder bed additive manufacturing process using a trained computer vision algorithm. Additive Manuf 19:114–126. https://doi.org/10.1016/j.addma.2017.11.009
145. Jin Z, Zhang Z, Gu GX (2019) Autonomous in-situ correction of fused deposition modeling printers using computer vision and deep learning. Manuf Lett 22:11–15. https://doi.org/10.1016/j.mfglet.2019.09.005
146. Liu Q, Wu H, Paul MJ, He P, Peng Z, Gludovatz B, Kruzic JJ, Wang CH, Li X (2020) Machine-learning assisted laser powder bed fusion process optimization for AlSi10Mg: new microstructure description indices and fracture mechanisms. Acta Mater 201:316–328. https://doi.org/10.1016/j.actamat.2020.10.010
147. Ma L, Liu H, Williams M, Levine L, Ramazani A (2024) Integrating phase field modeling and machine learning to develop process-microstructure relationships in laser powder bed fusion of IN718. Metallogr Microstruct Anal 13:983–995. https://doi.org/10.1007/s13632-024-01130-w
148. Boillat E, Kolossov S, Glardon R, Loher M, Saladin D, Levy G (2004) Finite element and neural network models for process optimization in selective laser sintering. Proc Institution Mech Eng Part B: J Eng Manuf 218:607–614. https://doi.org/10.1243/0954405041167121
149. Zhu Q, Liu Z, Yan J (2021) Machine learning for metal additive manufacturing: predicting temperature and melt pool fluid dynamics using physics-informed neural networks. Comput Mech 67:619–635. https://doi.org/10.1007/s00466-020-01952-9
150. Ren K, Chew Y, Zhang Y, Fuh J, Bi G (2020) Thermal field prediction for laser scanning paths in laser aided additive manufacturing by physics-based machine learning. Comput Methods Appl Mech Eng 362:112734. https://doi.org/10.1016/j.cma.2019.112734
151. Du Y, Mukherjee T, DebRoy T (2021) Physics-informed machine learning and mechanistic modeling of additive manufacturing to reduce defects. Appl Mater Today 24:101123. https://doi.org/10.1016/j.apmt.2021.101123